

## Magnetorotational Instability in Protoplanetary Disks. II. Ionization State and Unstable Regions

Takayoshi Sano<sup>1</sup>, Shoken M. Miyama

National Astronomical Observatory, Mitaka, Tokyo 181-8588, Japan

Toyoharu Umebayashi

Computing Service Center, Yamagata University, Yamagata 990-8560, Japan

and

Takenori Nakano

Department of Physics, Kyoto University, Sakyo-ku, Kyoto 606-8502, Japan

### ABSTRACT

We investigate where in protoplanetary disks magnetorotational instability operates, which can cause angular momentum transport in the disks. We investigate the spatial distribution of various charged particles and the unstable regions for a variety of models for protoplanetary disks taking into account the recombination of ions and electrons at grain surfaces, which is an important process in most parts of the disks. We find that for all the models there is an inner region which is magnetorotationally stable due to ohmic dissipation. This must make the accretion onto the central star non-steady. For the model of the minimum-mass solar nebula, the critical radius, inside of which the disk is stable, is about 20 AU, and the mass accretion rate just outside the critical radius is  $10^{-7} - 10^{-6} M_{\odot} \text{ yr}^{-1}$ . The stable region is smaller in a disk of lower column density. Dust grains in protoplanetary disks may grow by mutual sticking and may sediment toward the midplane of the disks. We find that the stable region shrinks as the grain size increases or the sedimentation proceeds. Therefore in the late evolutionary stages, protoplanetary disks can be magnetorotationally unstable even in the inner regions.

*Subject headings:* accretion, accretion disks — diffusion — instabilities — MHD — planetary systems — solar system: formation

---

<sup>1</sup>present address: Department of Astronomy, University of Maryland, College Park, MD 20742-2421; sano@astro.umd.edu

## 1. INTRODUCTION

Various infrared and radio observations have revealed the existence of accretion disks around T Tauri stars, so-called protoplanetary disks, where planet formation may be going on (e.g., Rucinski 1985; Adams, Lada, & Shu 1987). Photometric observations at optically thin millimeter wavelengths give disk masses of  $\sim 0.1 - 0.01 M_{\odot}$  (Beckwith et al. 1990), and fitting of spectral energy distributions (SEDs) at infrared wavelengths gives disk sizes of tens of AU or 100 AU (Adams, Lada, & Shu 1988). Some authors tried to reproduce the SEDs of T Tauri stars with models of viscous accretion disks (e.g., Bertout, Basri, & Bouvier 1988), and succeeded in deriving the slopes of SEDs at infrared wavelengths for some T Tauri stars. Optical and ultraviolet veiling of absorption lines has been discovered for some T Tauri stars, which indicates the existence of boundary layers at the interface between a Keplerian accretion disk and a slowly spinning star (Lynden-Bell & Pringle 1974). All these suggest the existence of accreting matter in protoplanetary disks at least in their early active stages. However, the mechanisms of angular momentum transport, necessary for accretion, have not yet been well understood, any more than in other astrophysical accretion disks.

The magnetorotational instability must be the most promising source of anomalous viscosity in accretion disks (Balbus & Hawley 1998, and references therein). Balbus & Hawley (1991) showed that astrophysical accretion disks are unstable to axisymmetric disturbances in the presence of a weak magnetic field. The instability sets in under a broad range of conditions and is capable of initiating and sustaining MHD turbulence in accretion disks, as long as the approximation of the ideal MHD holds. However, protoplanetary disks are so cold and dense that the ionization fraction is very low (Umebayashi & Nakano 1988). Because the coupling of some charged particles with magnetic fields is not strong enough, both the processes of ambipolar diffusion and ohmic dissipation have to be considered (Nakano 1984). These processes have an effect of suppressing the magnetorotational instability. It is necessary to clarify which parts of the disks are magnetorotationally unstable in relation to the evolution of protoplanetary disks.

Blaes & Balbus (1994) examined the effect of the ambipolar diffusion on the instability, and showed that differentially rotating disks are unstable when the collision frequency of neutral particles with ions exceeds the local epicyclic frequency. Sano & Miyama (1999, hereafter Paper I) investigated the stability of weakly ionized disks including the effect of ohmic dissipation. This process dominates the ambipolar diffusion in the regions of higher density, or in the inner parts (within about 100 AU) of the disks.

In paper I, we derived the conditions for the existence of unstable modes by the global linear analysis taking into account the effect of the vertical structure of the disks. The wavelength of the most unstable mode expected from the local linear analysis is approximately given by

$$\lambda_{\text{local}} \approx \max \left( 2\pi \frac{v_A}{\Omega}, 2\pi \frac{\eta}{v_A} \right), \quad (1)$$

where  $v_A = B/(4\pi\rho)^{1/2}$  is the Alfvén speed,  $\Omega$  is the angular rotational velocity of the disk, and  $\eta$  is the magnetic diffusivity (Jin 1996; Paper I). If the magnetic Reynolds number  $R_m \equiv v_A^2/\eta\Omega$  is larger than unity, the ohmic dissipation is not efficient and the wavelength of the most unstable

mode is approximately given by  $2\pi v_A/\Omega$ , which is the result of the ideal MHD. When  $R_m \lesssim 1$ , on the other hand, perturbations with shorter wavelengths are stabilized due to the dissipation. Thus, as the magnetic diffusivity increases,  $2\pi\eta/v_A$  increases and finally becomes the wavelength of the most unstable mode.

The local analysis gives the wavelength  $\lambda_{\text{local}}$  of the most unstable mode as a function of the local values of  $v_A$  and  $\eta$ . Thus  $\lambda_{\text{local}}$  takes different values at different points in the disk. Our results of the global analysis show that the vertical distribution of the wavelength  $\lambda_{\text{local}}(z)$  is quite important for the understanding of the global stability. In paper I, we have found that the layer at a height  $z$  is globally unstable when  $\lambda_{\text{local}}(z)$  obtained by the local analysis is shorter than the scale height of the disk  $H$ , or

$$\lambda_{\text{local}}(z) \approx \max \left[ 2\pi \frac{v_A(z)}{\Omega}, 2\pi \frac{\eta(z)}{v_A(z)} \right] \lesssim H. \quad (2)$$

The condition given by equation (2) agrees with the idea that the stability criterion is approximately given by the requirement that the shortest wavelength for local instability is smaller than the scale height of the disk.

Thus the ratio  $\lambda_{\text{local}}/H$  is a good indicator for the existence of global unstable modes. This ratio is sensitive to the magnetic diffusivity, which is determined by the physical quantities in protoplanetary disks such as the density, the temperature, and the ionization fraction. Umebayashi & Nakano (1988) examined the radial distribution of magnetic diffusivity on the midplane for the so-called minimum-mass solar nebula proposed by Hayashi, Nakazawa, & Nakagawa (1985). However, to make use of equation (2) as the stability criterion of protoplanetary disks, we have to know the vertical distribution of magnetic diffusivity. In this paper we investigate the two-dimensional distribution of magnetic diffusivity for various disk models, and reveal where in protoplanetary disks the magnetorotational instability is operative.

Because the recombination processes are more effective in denser regions, the ionization fraction is lower at higher density. Thus the inner dense region of the disks would be decoupled from magnetic fields except for the innermost region where the thermal ionization is efficient. However, even in the inner dense region, the gas near the surface layer of the disks may be well ionized because the density is low. Gammie (1996) proposed a layered accretion model which has the decoupled region (dead zone) sandwiched by the ionized active layers. The ionization by X-rays from the central object would also make a similar structure (Glassgold, Najita, & Igea 1997). In such situations, the column densities of the active layers are one of the most important quantities for the dynamical evolution of protoplanetary disks. We shall calculate the column densities of these layers and compare them with the previous works.

The recombination of ions and electrons on grain surface is the dominant process in the dense region. Therefore the characters of dust grains affect significantly the ionization fraction and the column density of the active layers. In the previous works grain surface reactions were not included because they were concerned mainly in the late phases of the disks when dust grains of the disks have already settled toward the midplane. In this paper we investigate the effect of dust grains on the abundances of charged particles and the contribution of charged grains to the interaction

of the gas with magnetic fields in protoplanetary disks, and show where the magnetorotational instability can be operative.

The plan of this paper is as follows. In §2 we describe the disk models adopted in this paper and the magnetic diffusivity of the gas composed of various kinds of charged particles. We also describe the reaction scheme which determines the abundance of charged particles in ionization-recombination equilibrium. In §3 we show numerical results on the spatial distribution of charged particles, the time scale of magnetic field dissipation, and the unstable regions in the disks. Because charged grains can be the dominant charged particles at least in some parts of the protoplanetary disks, their size and abundance are highly important in determining the magnetic diffusivity. Dust grains may grow by mutual sticking. They will sediment onto the midplane if the disk is quiescent. The coupling between the gas and magnetic field varies as the disk evolves in such ways. In §3 we also examine the unstable regions in some model disks which must correspond to different evolutionary stages. In §4 we investigate the column densities of active layers and discuss the evolutionary scenario of protoplanetary disks taking account of the magnetorotational instability. We also discuss the validity of our assumptions and some related problems in §4. Finally we summarize our results in §5.

## 2. MODEL AND FORMULATION

### 2.1. Structure of Protoplanetary Disks

Although various models have been proposed for protoplanetary disks, there seem to be no really acceptable models yet. In view of such a situation we will investigate on a variety of models and find out some firm results. The surface density  $\Sigma(r)$  of the protoplanetary disks is one of the most important quantities in constructing the disk models. We assume a power-law distribution

$$\Sigma(r) = \Sigma_0 \left( \frac{r}{1 \text{ AU}} \right)^{-q}, \quad (3)$$

where  $r$  is the distance from the central star. Hayashi (1981) found that the surface density of the primitive solar nebula, which is restored from the mass distribution in the present solar system, is well represented by equation (3) with  $q = 3/2$  and  $\Sigma_0 \approx 1.7 \times 10^3 \text{ g cm}^{-2}$ . This model is thus called the minimum-mass solar nebula. We examine mainly for the models with  $q = 3/2$  and  $\Sigma_0 = 1.7 \times 10^3 f_\Sigma \text{ g cm}^{-2}$  in this paper, where  $f_\Sigma$  is an arbitrary parameter. Equation (3) in this case must break down at large  $r$  because the total mass of the disk should not diverge. In this work we examine the regions of  $r \lesssim 100 \text{ AU}$ . Because the power index  $q$  could take different values (e.g., Cassen 1994), we will also investigate for the other values of  $q$ .

For the temperature of the disks we also assume a power-law distribution,

$$T(r) = T_0 \left( \frac{r}{1 \text{ AU}} \right)^{-p}. \quad (4)$$

Except for a very early accretion phase, the temperature of the disk is determined by the energy balance between absorption of stellar radiation and emission of thermal radiation. After dust

grains in the disk have sunk toward the midplane to some extent, most part of the disk is nearly transparent to the stellar light and the thermal radiation. The equilibrium temperature in such a situation is given by  $p = 1/2$  and  $T_0 = 280$  K for the luminosity of the central star  $L_* = 1 L_\odot$ . We adopt  $p = 1/2$  and  $T_0 = 280$  K even for the opaque regions near the midplane because it may be regarded as being in a thermal bath of this temperature. For simplicity we also adopt this temperature distribution even for the early opaque stage before significant sedimentation of dust grains occurs because the results are not very sensitive to the temperature as long as it is below several hundred Kelvin (see §4.5). With  $p = 1/2$  and  $T_0 = 280$  K, the sound velocity is given by

$$c_s(r) = \left( \frac{kT}{\mu m_H} \right)^{1/2} = 9.9 \times 10^4 \left( \frac{r}{1 \text{ AU}} \right)^{-1/4} \left( \frac{\mu}{2.34} \right)^{-1/2} \text{ cm sec}^{-1}, \quad (5)$$

where  $k$  is the Boltzmann constant,  $\mu$  is the mean molecular weight of the gas, and  $m_H$  is the mass of a hydrogen atom.

In a gravitationally stable disk, the gravity perpendicular to the disk is mainly contributed by the central star. The balance of the stellar gravity and the pressure force in the  $z$ -direction determines the gas density at height  $z$  from the midplane as

$$\rho(r, z) = \rho_c(r) \exp \left[ -\frac{z^2}{H^2(r)} \right], \quad (6)$$

where  $\rho_c(r)$  is the density at the midplane and

$$H(r) = \frac{\sqrt{2}c_s}{\Omega} \quad (7)$$

is the scale height of the disk. For the Keplerian angular velocity  $\Omega = (GM_*/r^3)^{1/2}$ , where  $G$  is the gravitational constant and  $M_*$  is the mass of the central star, the density at the midplane is given by

$$\rho_c(r) = 1.4 \times 10^{-9} f_\Sigma \left( \frac{r}{1 \text{ AU}} \right)^{-11/4} \left( \frac{M_*}{M_\odot} \right)^{1/2} \left( \frac{\mu}{2.34} \right)^{1/2} \text{ g cm}^{-3}, \quad (8)$$

for  $\Sigma$  given by equation (3) with  $q = 3/2$  and for  $c_s$  given by equation (5).

The local stability analysis shows that a disk rotating around a star with the Keplerian velocity is gravitationally stable only when  $\Sigma < \Omega c_s / \pi G$  (Goldreich & Lynden-Bell 1965). The disk given by equations (3) and (5) with  $q = 3/2$  is gravitationally stable when the inequality,

$$f_\Sigma < 17.5 \left( \frac{r}{100 \text{ AU}} \right)^{-1/4} \left( \frac{M_*}{M_\odot} \right)^{1/2} \left( \frac{\mu}{2.34} \right)^{-1/2}, \quad (9)$$

is fulfilled. Since we are concerned with gravitationally stable disks of radius  $r \lesssim 100$  AU, it is sufficient to consider the cases of  $f_\Sigma \lesssim 10$ .

## 2.2. Magnetic Diffusivity

The magnetic diffusivity  $\eta$  is given in terms of the electrical conductivity  $\sigma_c$  and the light speed  $c$  by

$$\eta = \frac{c^2}{4\pi\sigma_c}. \quad (10)$$

The electrical conductivity is given by

$$\sigma_c = \sum_{\nu} \frac{(eq_{\nu})^2 \tau_{\nu} n_{\nu}}{m_{\nu}}, \quad (11)$$

where  $\tau_{\nu}$  is the viscous damping time of motion relative to neutral particles of a charged particle  $\nu$  with mass  $m_{\nu}$  and electric charge  $eq_{\nu}$ , and  $n_{\nu}$  is the number density of particle  $\nu$ .

Because the mass of an ion,  $m_i$ , is generally much greater than the mass of a neutral molecule,  $m_n$ , we have for an ion

$$\tau_i^{-1} = n_n \langle \sigma v \rangle_i \frac{m_n}{m_i}, \quad (12)$$

where  $n_n$  is the number density of neutrals and  $\langle \sigma v \rangle_i$  is the rate coefficient for the collision between ions and neutrals averaged over the distribution of the relative velocity. The momentum-transfer cross section of a singly charged ion due to electrical polarization force is given by (Osterbrock 1961)

$$\sigma = 2.41\pi \left( \frac{\alpha e^2}{mv^2} \right)^{1/2}, \quad (13)$$

where  $\alpha$  is the polarizability of a neutral molecule,  $e$  is the elementary electric charge,  $m$  is the reduced mass, and  $v$  is the relative velocity. Almost all ions at such low temperatures are singly charged. We have  $\alpha = 7.9 \times 10^{-25} \text{ cm}^3$  for an  $\text{H}_2$  molecule and  $\alpha = 2.1 \times 10^{-25} \text{ cm}^3$  for a He atom. By taking the mass of an ion  $m_i \approx 34 m_{\text{H}}$ , for example, we have  $\langle \sigma v \rangle_{i-\text{H}_2} \approx 1.8 \times 10^{-9} \text{ cm}^3 \text{ s}^{-1}$ , which is independent of  $v$  as long as  $\sigma$  is larger than the geometrical cross section. Such a rate coefficient due to polarization force is called the Langevin's rate coefficient.

For an electron we have

$$\tau_e^{-1} = n_n \langle \sigma v \rangle_e. \quad (14)$$

In the previous works, the Langevin's rate was also used for the rate coefficient for the collision between electrons and neutrals. However, the collision cross sections obtained by experiments at low electron energies are much smaller than  $\sigma$  given by equation (13) and is nearly equal to a geometrical cross section. In this paper, we use the cross sections recommended by M. Hayashi (1981) who compiled the experimental results (see Appendix).

We neglect the contribution of electron-ion collisions to the electrical conductivity in equation (11). The contribution of electron-ion collision is  $\tau_e/\tau_{e-i}$  times the contribution of electron-neutral collision, where  $\tau_{e-i}$  is the collision time of an electron with ions, and is inefficient unless  $n_e/n_n > 10^{-8}$  and  $10^{-4}$  at  $T = 10$  and  $10^3$  K, respectively.

For a grain of any charge, we have

$$\tau_g^{-1} = n_n \langle \sigma v \rangle_g \frac{m_n}{m_g}, \quad (15)$$

where  $m_g$  is the mass of a grain. Because the mean free path of neutrals is much greater than the size of a grain, we have for a spherical grain of radius  $a$ ,

$$\langle \sigma v \rangle_g = \frac{4\pi}{3} a^2 c_{\text{th}}, \quad (16)$$

where  $c_{\text{th}} = (8kT/\pi\mu m_{\text{H}})^{1/2}$  is the thermal velocity of a neutral molecule.

### 2.3. Reaction Scheme

We investigate numerically the densities of various kinds of charged particles in order to calculate the magnetic diffusivity  $\eta$  given by equation (10). The rate equation for a constituent  $X_i$  is given by

$$\frac{dn(X_i)}{dt} = \sum_j \gamma_{ij} n(X_j) + \sum_{j,k} \beta_{ijk} n(X_j) n(X_k) , \quad (17)$$

where  $n(X_i)$  is the number density of  $X_i$ ,  $\gamma_{ij}$  is the rate coefficient for forming  $X_i$  by ionization of  $X_j$ , and  $\beta_{ijk}$  is the rate coefficient of a two-body reaction including reactions on dust grains. Because the gas in protoplanetary disks can be regarded as being in ionization-recombination equilibrium (see §4.6 below), equation (17) is reduced to

$$\sum_j \frac{\gamma_{ij}}{n_H} x(X_j) + \sum_{j,k} \beta_{ijk} x(X_j) x(X_k) = 0 , \quad (18)$$

where  $x(X_i) \equiv n(X_i)/n_H$ . We solve equation (18) at each position of the disk to obtain the spatial distribution of magnetic diffusivity.

We consider the regions of the disk where the temperature is less than several hundred Kelvin, and thus the thermal ionization is inefficient compared with the ionization by non-thermal particles (Umebayashi 1983; Nakano & Umebayashi 1988). In such regions ions and electrons are produced mainly through ionization by cosmic rays and radioactivity, and vanish through various recombination processes. Since these situations are quite similar to those in very dense interstellar clouds, we adopt a simplified reaction scheme for dense clouds investigated by Umebayashi & Nakano (1980, 1990) and Nishi, Nakano, & Umebayashi (1991) with some modifications. Among the modifications are updating the reaction rates and adding some species of charged particles such as  $H_2^+$  and grains of charge  $\pm 3e$ . We also take into account the electrical polarization of grains for collisions with ions and electrons. In the following we describe the reaction scheme adopted in this paper.

#### 2.3.1. Reactions in Gas Phase

The elements to be considered in our reaction scheme are H, He, C, O, and refractory heavy elements. We adopt the solar system abundances for these elements (Anders & Grevesse 1989) which are shown in Table 1. Most of the heavy elements have condensed in dust grains and only a small fraction of them remain in the gas phase. We denote this fraction as  $\delta_1$  for the volatile elements C and O, and  $\delta_2$  for the refractory heavy elements. We assume for simplicity that all grains have the same size unless otherwise stated. Then the grain abundance  $n_g/n_H$  by number relative to hydrogen is determined from the total amounts of those elements in grains.

We can regard that each element in gas phase has been transformed into its molecular form because we consider low temperature, high density regions. We assume that all C in the gas phase is in CO molecule. Oxygen in the gas phase other than the constituent of CO is in the form of  $O_2$ ,  $H_2O$ , OH, or O. Since the reaction rate coefficients of molecules  $O_2$ ,  $H_2O$ , and OH with ions are of

the same order and the recombination rate coefficients of the resultant ions with electrons are also of the same order, we regard the reactions of the most abundant species  $\text{O}_2$  as the representatives of their reactions. We introduce a parameter  $f_{\text{O}_2}$  which represents the fraction of oxygen in the gas phase in the molecular form  $\text{O}_2$ ,  $\text{H}_2\text{O}$ , and  $\text{OH}$ . Because the metal atoms such as Na, Mg, and Al have nearly the same rate coefficients for charge-transfer reaction with molecular ions and the resultant metal ions also have similar rate coefficients for radiative recombination with electrons, we neglect the differences among them and denote them as M collectively.

We consider the following species of charged particles in our reaction scheme: electron  $e$ ,  $\text{H}^+$ ,  $\text{He}^+$ ,  $\text{C}^+$ ,  $\text{H}_2^+$ ,  $\text{H}_3^+$ , molecular ion  $m^+$  (except  $\text{H}_2^+$  and  $\text{H}_3^+$ ), metal ion  $\text{M}^+$ , and charged grains. Dust grains in the disks can be charged through the collision with electrons and ions in the gas phase. We consider the grains of charge 0 (neutral),  $\pm 1e$ ,  $\pm 2e$ , and  $\pm 3e$ . Table 2 shows the reactions in gas phase and their rate coefficients (Millar, Farquhar, & Willacy 1997). The important reactions of molecular ions  $m^+$  are dissociative recombination with electrons and charge transfer with metal atoms. Because the rate coefficients of these reactions are similar among various molecular ions, we regard all  $m^+$  as a single species. For the rate coefficients of  $m^+$ , we use those of the most abundant ion,  $\text{HCO}^+$ . Similarly, we regard the rate coefficients of  $\text{Mg}^+$  as the representatives of those of metal ions  $\text{M}^+$ .

### 2.3.2. Reactions on Grain Surfaces

Dust grains may gradually settle to a very thin layer about the midplane reducing the grain abundance in the major part of the disk (Nakagawa, Nakazawa, & Hayashi 1981). We define a parameter  $f_g$  that represents the abundance of dust grains relative to that in molecular clouds. The depletion parameter  $f_g$  may be regarded as representing the evolutionary stage of the disk.

For simplicity, we assume that all dust grains have the same size (radius)  $a$ , and that they consist of rocky and metallic materials. We take the inner density of grain material as  $3 \text{ g cm}^{-3}$ . We discuss the effects of the grain-size distribution and the effect of tiny grains in §3.3. We neglect icy material ( $\text{H}_2$ ,  $\text{CH}_4$ , and  $\text{NH}_3$ ) in dust grains because they have only small effects on the ionization state of the disk (Umebayashi 1983).

At the low temperatures concerned in this work, dust grains can adsorb ions and electrons. Thus, in addition to the radiative and dissociative recombinations of ions and free electrons in the gas phase, we have to take into account their recombination on grain surfaces, which occurs through grain-ion, grain-electron, and grain-grain collisions. As in the previous works (Nakano 1984; Umebayashi & Nakano 1990; Nishi et al. 1991), we adopt the following model for the reactions on grain surfaces:

1. When an ion hits a neutral grain or a positively charged grain, it sticks to the grain with a probability  $S_i \approx 1$ . The sticking probability  $S_e$  of an electron onto a neutral or negatively charged grain has been found to be between 0.2 and 1.0 (Nishi et al. 1991). We use  $S_e = 0.6$  as in the previous works.



2. When an ion hits a negatively charged grain, or an electron hits a positively charged grain, the electron and the ion recombine and leave the grain surface using the energy released by the recombination.
3. When grains of opposite charge collide in thermal Brownian motion, they neutralize themselves. We neglect coalescence of grains.

We take account of the effect of electrical polarization of grains for the collision with an ion or an electron by using the fitting formula for the collision rate coefficient obtained by Draine & Sutin (1987).

### 2.3.3. Ionization Processes

In protoplanetary disks, charged particles are formed first by ionization of  $\text{H}_2$  and He by cosmic rays and radioactive elements. Table 3 lists the reaction rates of  $\text{H}_2$  and He with such energetic particles in units of the total ionization rate  $\zeta$  of a hydrogen molecule, which includes the ionization by secondary electrons. The ionization rate in the disk is effectively given by

$$\zeta(r, z) \approx \frac{\zeta_{\text{CR}}}{2} \left[ \exp\left(-\frac{\chi(r, z)}{\chi_{\text{CR}}}\right) + \exp\left(-\frac{\Sigma(r) - \chi(r, z)}{\chi_{\text{CR}}}\right) \right] + \zeta_{\text{R}}, \quad (19)$$

where  $\zeta_{\text{CR}} \approx 1.0 \times 10^{-17} \text{ sec}^{-1}$  is the ionization rate by cosmic rays in the interstellar space, and  $\zeta_{\text{R}} \approx 6.9 \times 10^{-23} f_{\text{g}} \text{ sec}^{-1}$  is the ionization rate by radioactive elements contained in the disk (Umebayashi & Nakano 1981). The depth

$$\chi(r, z) = \int_z^{\infty} \rho(r, z) dz \quad (20)$$

is the vertical column density from infinity to the position concerned. The attenuation length of the ionization rate by cosmic rays has a value  $\chi_{\text{CR}} \approx 96 \text{ g cm}^{-2}$  (Umebayashi & Nakano 1981). Because most of the radioactive elements are in rocky and metallic materials, the rate  $\zeta_{\text{R}}$  is proportional to the depletion factor  $f_{\text{g}}$  of dust grains.

## 3. RESULTS

### 3.1. The Minimum-Mass Solar Nebula — The Fiducial Model

First, we investigate the stability of a disk rotating around a star of  $M_* = 1 M_{\odot}$  with the surface density parameter  $f_{\Sigma} = 1$ , which we presume to well represent the primitive solar nebula. We take  $p = 1/2$  and  $T_0 = 280 \text{ K}$  in equation (4). We adopt the radius of dust grains  $a = 0.1 \mu\text{m}$  and the grain depletion factor  $f_{\text{g}} = 1$  corresponding to early evolutionary stages where sedimentation of dust grains has hardly proceeded yet. We assume  $\delta_1 = 0.2$  and  $\delta_2 = 0.02$  for the parameters of element depletion, and we adopt  $f_{\text{O}_2} = 0.7$  in accordance with the results of Mitchell, Kuntz, & Ginsburg (1978) on the calculation of molecular abundances. We call this the fiducial model.

### 3.1.1. Spatial Distribution of Charged Particles

Figure 1 shows the distribution of relative abundances  $n(X)/n_{\text{H}}$  of some representative particles X on the midplane for the fiducial model. The ionization rate at the midplane is also shown in the upper panel as a function of the radius  $r$ . Figure 2 shows the resulting electrical conductivity  $\sigma_c$  given by equation (11). The abundances of charged particles and the electrical conductivity decrease as the distance from the central star decreases. When the time scale of magnetic field dissipation,

$$t_{\text{dis}} \approx \frac{H^2}{\eta}, \quad (21)$$

is comparable to or smaller than the Keplerian orbital period  $t_{\text{K}} = 2\pi/\Omega$ , magnetic fields are almost decoupled from the gas. We call the distance from the central star at which  $t_{\text{dis}} = t_{\text{K}}$  holds the decoupling radius  $r_{\text{dec}}$ . Figure 3 depicts the ratio of the dissipation time  $t_{\text{dis}}$  to the dynamical time  $t_{\text{K}}$  as a function of  $r$ . We find  $t_{\text{dis}} \lesssim t_{\text{K}}$  at  $r < r_{\text{dec}} \approx 15$  AU, where the hydrogen number density  $n_{\text{H}}$  is higher than  $10^{12} \text{ cm}^{-3}$ .

In the region of  $r \gtrsim r_{\text{dec}}$ , electrons and metal ions are the dominant charged particles as seen from Figure 1. Electrons and ions recombine mainly by collision with dust grains, and thus the relative abundances are inversely proportional to  $n_{\text{H}}$ . The conductivity is mainly contributed by electrons, and is proportional to  $x(\text{e})$ .

In the region of  $r \lesssim r_{\text{dec}}$ , on the other hand, the number density of dust grains is higher than that of ions, and the dust grains with charge  $\pm e$  are the dominant charged particles. Because the charge neutrality must be kept mainly by grains, or  $n(\text{G}(+1)) \approx n(\text{G}(-1))$ , the number density of free electrons  $n(\text{e})$  becomes considerably lower than that of metal ions  $n(\text{M}^+)$ . The ratio  $n(\text{e})/n(\text{M}^+)$  approaches the limiting value  $(m_e/S_e m_{\text{M}})^{1/2}$  (Umebayashi 1983; Nakano 1984) as  $r$  decreases from 10 AU, where  $m_e$  and  $m_{\text{M}}$  are masses of electron and metallic ion, respectively. At  $r \lesssim 7$  AU, the column density of the disk exceeds the attenuation length of cosmic rays,  $\chi_{\text{CR}}$ , and the abundance of charged particles reduces considerably due to decrease of the ionization rate. In the region of  $r \lesssim 2$  AU, where the terrestrial planets orbit in the present solar system, the abundances of dust grains with electric charge  $\pm e$  decrease as  $r$  decreases. This is due to recombination of adsorbed electrons and ions during grain-grain collision. At  $r \lesssim 1$  AU, where the number density of ions is more than  $10^4$  times smaller than that of charged grains, the contribution to  $\sigma_c$  is dominated by charged grains as seen in Figure 2.

We next investigate the abundances of charged particles and the dissipation time of magnetic field off the midplane at some representative regions. Figure 4 depicts the relative abundances of some representative particles as functions of the height  $|z|$  from the midplane for the region  $r = 1$  AU where the Earth may have formed. As  $|z|$  decreases, the abundances of charged particles decrease, and as a result the electrical conductivity also decreases. At  $|z| \lesssim 3.0 H$ , the number density of free electrons deviates from that of metal ions, and dust grains with electric charge  $\pm e$  are the dominant charged particles. At  $|z| \lesssim 1.0 H$ , the number density of charged grains decreases as  $|z|$  decreases because of the charge neutralization by mutual collisions. The conductivity is mainly contributed by ions and electrons except at  $|z| \lesssim 0.1 H$  where the number density of ions is lower than  $10^{-4}$  times that of charged grains.

Figure 5 shows the relative abundances of some representative particles for another typical region  $r = 30$  AU where Neptune may have formed. Because of the low density  $n_H \lesssim 10^{10} \text{ cm}^{-3}$ , electrons and metal ions are the dominant charged particles at any height.

Figure 6 shows the dissipation time  $t_{\text{dis}}$  as a function of  $|z|$  at  $r = 1$  and 30 AU. In the region  $r = 1$  AU  $t_{\text{dis}}$  is smaller than the dynamical time  $t_K$  at  $|z| \lesssim z_{\text{dec}} \approx 3.2 H$  where the number density  $n_H$  exceeds  $10^{11} \text{ cm}^{-3}$ . Notice that the column density of the well-coupled region, where  $t_{\text{dis}} > t_K$  holds, is smaller than  $10^{-2} \text{ g cm}^{-2}$ , which is much less than the attenuation length of cosmic rays  $\chi_{\text{CR}}$ , and as a result  $\zeta \approx \zeta_{\text{CR}}$  as shown in the upper panel of Figure 4, different from Gammie (1996). The low ionization fraction in the decoupled regions is caused merely by the very high density, not by attenuation of cosmic rays. At  $r = 30$  AU we find  $t_{\text{dis}} \gg t_K$  at any  $z$ , and consequently the gas is strongly coupled with magnetic fields.

### 3.1.2. Unstable Regions

We shall find out the regions where the condition given by equation (2) is satisfied using the spatial distribution of magnetic diffusivity on the  $r$ - $z$  plane obtained above. In such regions, the magnetorotational instability is operative (Paper I), and thus we call them the unstable regions.

Since the stability condition also depends on the Alfvén speed, we have to specify the spatial distribution of magnetic field strength. For the sake of simplicity, we consider only the vertical component of magnetic fields, and assume that the plasma beta at the midplane,  $\beta_c = 2c_s^2/v_{\text{Ac}}^2$ , is constant in the disk, where  $v_{\text{Ac}}$  is the Alfvén speed at the midplane. Then, the distribution of magnetic field strength for the disks with  $q = 3/2$ ,  $M_* = 1 M_\odot$ ,  $p = 1/2$ , and  $T_0 = 280$  K is given by

$$B(r) = 1.9 f_\Sigma^{1/2} \left( \frac{r}{1 \text{ AU}} \right)^{-13/8} \left( \frac{\beta_c}{100} \right)^{-1/2} \text{ G} . \quad (22)$$

Figures 7a and 7b show the unstable regions for the cases of  $\beta_c = 100$  and 1000, respectively. In these figures the curve labeled  $\lambda_{\text{ideal}}/H = 1$  represents the locus of the points at which the characteristic unstable wavelength in the ideal MHD limit,  $\lambda_{\text{ideal}}$ , is equal to the scale height of the disk,

$$\lambda_{\text{ideal}}(r, z) \equiv 2\pi \frac{v_A(r, z)}{\Omega(r)} = H(r) . \quad (23)$$

The curve with  $\lambda_{\text{res}}/H = 1$  is the locus of the points at which the characteristic unstable wavelength in the resistive limit,  $\lambda_{\text{res}}$ , is equal to the scale height,

$$\lambda_{\text{res}}(r, z) \equiv 2\pi \frac{\eta(r, z)}{v_A(r, z)} = H(r) . \quad (24)$$

The critical condition for decoupling of magnetic field,  $t_{\text{dis}} = t_K$ , mentioned above is equivalent to equation (24) when  $\beta_c = 1$ .

For a given radius,  $\lambda_{\text{ideal}}$  increases exponentially as the height  $|z|$  increases because the Alfvén speed becomes greater, while  $\lambda_{\text{res}}$  decreases because the magnetic diffusivity decreases as  $|z|$

increases. Therefore, the instability condition  $\max(\lambda_{\text{ideal}}, \lambda_{\text{res}}) \lesssim H$  [eq. (2)] is satisfied only in the striped area between the two critical curves  $\lambda_{\text{ideal}}/H = 1$  and  $\lambda_{\text{res}}/H = 1$  in Figure 7.

The condition  $\lambda_{\text{ideal}}/H = 1$  is easily reduced to

$$|z| = \left( \ln \frac{\beta_c}{4\pi^2} \right)^{1/2} H, \quad (25)$$

which gives  $|z| = 0.96 H$  and  $1.8 H$  for  $\beta_c = 100$  and  $1000$ , respectively. The magnetorotational instability is suppressed due to magnetic dissipation in the region below the critical curve  $\lambda_{\text{res}}/H = 1$ , which corresponds to Gammie’s (1996) “dead zone”. The dissipation process is less important for stronger magnetic field. Thus the stable region shrinks as the plasma beta decreases. At the points where  $\lambda_{\text{res}}/H = 1$  holds, the hydrogen number density  $n_{\text{H}}$  takes  $0.8 - 1.7 \times 10^{11}$  and  $0.5 - 1.2 \times 10^{11} \text{ cm}^{-3}$  for the cases of  $\beta_c = 100$  and  $1000$ , respectively. At temperatures below several hundred Kelvin where thermal ionization is negligible, the magnetic diffusivity is determined mainly by the density and the ionization rate. Because the column density above the dead zone is far below the attenuation length of cosmic rays, the boundary of the dead zone is determined mostly by the local density in this case.

The electrical conductivity is mainly contributed by electrons at the boundary of the dead zone. The relative abundance of electrons  $x(\text{e})$  at the boundary is  $1.1 - 2.7 \times 10^{-14}$  and  $2.8 - 7.1 \times 10^{-14}$  for the cases of  $\beta_c = 100$  and  $1000$ , respectively. The magnetic diffusivity is inversely proportional to  $x(\text{e})$  in such a situation, and then we approximately have  $x(\text{e}) \propto v_{\text{A}}^{-1}$  on the curve  $\lambda_{\text{res}}/H = 1$  at a given radius.

Let the critical radius  $r_{\text{crit}}$  be the outer radius of the dead zone on the midplane, which is about 19 and 22 AU for the cases of  $\beta_c = 100$  and  $1000$ , respectively. The region  $r \gtrsim r_{\text{crit}}$  is magnetorotationally unstable except at tenuous outer layers. In this region, because the magnetic field is amplified due to growth of fluctuations, the angular momentum can be transported effectively. As seen from Figure 7b, the unstable region exists even at  $r < r_{\text{crit}}$  above the dead zone. However, the column density of this unstable layer is so small that mass accretion cannot be as active as in the region  $r > r_{\text{crit}}$ . Therefore, the accreting matter from the outer region must accumulate near the outer boundary of the dead zone, unless some other mechanisms of angular momentum transport are effective.

In the following subsections, we shall depict the unstable regions on the  $r$ - $z$  plane for various disk models. The criterion given by equation (24) is more important than the criterion (23) because the critical radius on the midplane  $r_{\text{crit}}$  is determined by equation (24). Therefore, in the following we focus on the dead zone given by the criterion  $\lambda_{\text{res}}/H = 1$ . Because the results are not very sensitive to the plasma beta as seen from Figure 7, we show only the results for the cases of  $\beta_c = 100$  and  $1000$  in the following.

### 3.2. Disks with Various Surface Densities

### 3.2.1. Dependence on the Disk Mass

We investigate the disks with different surface densities rotating around a star of  $M_* = 1 M_\odot$ . We consider the following cases of the surface density parameter; (a)  $f_\Sigma = 0.3$ , (b)  $f_\Sigma = 1$  (the minimum-mass solar nebula), (c)  $f_\Sigma = 3$ , and (d)  $f_\Sigma = 10$ . Figure 8 shows the results for the cases with the depletion factor of dust grains  $f_g = 1$  corresponding to early evolutionary stages of the disks. The other parameters are the same as in the fiducial model. The solid and dashed curves in each panel represent the loci of  $\lambda_{\text{res}}/H = 1$  for the cases of  $\beta_c = 100$  and 1000, respectively. Inside these curves are the dead zones where the ohmic dissipation suppresses the magnetorotational instability. The dotted curve shows the scale height of the disk  $z = H(r)$ .

Because the dead zone has a height close to the scale height  $H$  for most part of  $r < r_{\text{crit}}$ , most of the matter at  $r < r_{\text{crit}}$  is in the region where the instability is suppressed. Because the ohmic dissipation is not so efficient as to suppress the magnetorotational instability outside the dead zones in Figure 8, magnetic fields are amplified to some extent by the instability and angular momentum transport due to magnetic stress is expected though mass accretion through the layers above the dead zones may not be efficient because of their low column densities.

We find that a higher mass disk is more stable for the magnetorotational instability; as the surface density parameter  $f_\Sigma$  increases, the dead zone expands and the critical radius  $r_{\text{crit}}$  increases. This is because the recombination processes are more effective in denser regions, and thus the ionization fraction is lower in higher mass disks. In the case of  $\beta_c = 100$  (1000), the critical radius on the midplane,  $r_{\text{crit}}$ , is 13 (16), 19 (22), 26 (31), and 39 (45) AU for  $f_\Sigma = 0.3, 1, 3$ , and 10, respectively. At the points where  $\lambda_{\text{res}}/H = 1$  holds, the hydrogen number density takes a value between a few  $\times 10^{10}$  and a few  $\times 10^{11} \text{ cm}^{-3}$  almost independent of  $f_\Sigma$ . Therefore, the boundary of the dead zone is determined mainly by the local density  $n_{\text{H}}$ ; cosmic rays are hardly attenuated at these points as in the fiducial model.

### 3.2.2. Dependence on the Power Index of $\Sigma$

So far we have considered only the disks with the power index of  $\Sigma$ ,  $q = 3/2$ . There are no definite observations that constrain surface density profiles of protoplanetary disks. Some of the extrasolar planet candidates discovered by radial velocity oscillation orbit within just 0.3 AU, suggesting that they have migrated inward after their birth (e.g., Marcy, Cochran, and Mayor 2000). Thus the mass distribution of the present-day solar system might be different from the primordial distribution. Here we examine some other models with different power index; (a)  $q = 2$ , (b)  $q = 3/2$  (fiducial model), (c)  $q = 1$ , and (d)  $q = 0$ . We assume that all these models have equal mass  $0.024 M_\odot$  between 0.1 and 100 AU. Thus the surface density at 1 AU is  $4.8 \times 10^3, 1.7 \times 10^3, 3.3 \times 10^2$ , and  $6.6 \text{ g cm}^{-2}$  for  $q = 2, 3/2, 1$ , and 0, respectively. The results for a disk of  $f_g = 1$  around a star of  $M_* = 1 M_\odot$  are shown in Figure 9. The other parameters are the same as in the fiducial model. The results are quite similar among these models though the critical radius  $r_{\text{crit}}$  takes somewhat different values. The critical radius on the midplane is mainly determined by the density which is about  $1.6 \times 10^{11}$  and  $1.1 \times 10^{11} \text{ cm}^{-3}$  for  $\beta_c = 100$  and 1000, respectively.

### 3.3. Disks in Some Evolutionary Stages

#### 3.3.1. Depletion of Dust Grains

The ionization fraction and the species of dominant charged particles are sensitive to the depletion factor of dust grains,  $f_g$ , the abundance of dust grains relative to that in molecular clouds. As the dust grains in a protoplanetary disk sink gradually toward the midplane,  $f_g$  decreases and the recombination rate on grain surfaces reduces except in a very thin layer around the midplane. As a result, the ionization fraction increases (Umebayashi & Nakano 1988) and the dead zone shrinks in the late evolutionary stages.

Figure 10 shows the relative abundances of some representative particles as functions of the height from the midplane at  $r = 1$  AU for the case of  $f_g = 10^{-4}$ . Electrons and metal ions are the dominant charged particles at any height  $z$  due to the low abundance of dust grains. Magnetic fields are well coupled with the gas in the larger part of the disk compared with the case of  $f_g = 1$ . The electrical conductivity  $\sigma_c$  is mainly contributed by electrons, and is proportional to  $x(e)$  at any  $z$ . At  $|z| \lesssim 1.0 H$ , the ionization by cosmic rays declines (upper panel of Fig. 10) because the depth  $\chi(r, z)$  exceeds the attenuation length of cosmic rays,  $\chi_{\text{CR}}$ . As seen from the dot-dashed curve in Figure 6, the ratio  $t_{\text{dis}}/t_K$  becomes less than unity at  $|z| \lesssim z_{\text{dec}} \approx 0.8 H$ , so that the gas decouples from magnetic fields in this region. This decoupled layer is significantly thinner than for the case of  $f_g = 1$ .

To clarify the effect of grain depletion, we investigate several cases with respect to the depletion factor of dust grains, (a)  $f_g = 1$  (fiducial model), (b)  $f_g = 10^{-1}$ , (c)  $f_g = 10^{-2}$ , and (d)  $f_g = 10^{-4}$ , each of which might correspond to some evolutionary stage of the protoplanetary disk. Figure 11 shows the results for the disk with the surface density parameter  $f_\Sigma = 1$  around a star of  $M_* = 1 M_\odot$ . The other parameters are the same as in the fiducial model.

We find that decrease of dust abundance makes smaller the region where magnetorotational instability is suppressed by ohmic dissipation. At later stages where only a very small fraction of the initial dust grains floats, magnetic fields are nearly frozen to the gas in most parts of the disk. This implies that the magnetorotational instability is operative at a larger part of the disk and the angular momentum transport is more effective in the later evolutionary stages. For the case of  $\beta_c = 100$ , the critical radius  $r_{\text{crit}}$  is 19, 7.6, 3.8, and 2.0 AU for the models of  $f_g = 1, 10^{-1}, 10^{-2}$ , and  $10^{-4}$ , respectively.

For  $f_g = 10^{-4}$ , the critical height  $z_{\text{crit}}$  where  $\lambda_{\text{res}}/H = 1$  holds is  $1.0 H$  and  $1.2 H$  for the cases of  $\beta_c = 100$  and  $1000$ , respectively, at 1 AU. At these points, electrons and metal ions are still dominant charged particles (see Fig. 10). At  $|z| = z_{\text{crit}}$  in the region of  $r \approx 1$  AU, the ionization rate is smaller than  $\zeta_{\text{CR}}$  by an order of magnitude. This is because the column density above the dead zone is nearly equal to  $\chi_{\text{CR}} \approx 96 \text{ g cm}^{-2}$  for these cases.

### 3.3.2. Growth of Grains

The interstellar grains have a wide size distribution, e.g., between 0.005 and 0.25  $\mu\text{m}$  (Mathis, Rumpl, & Nordsieck 1977; hereafter MRN). By coalescence of dust grains in protoplanetary disks, the size distribution and the relative number density of grains may change considerably. To clarify the effect of grain size on the unstable regions, we investigate the following four cases assuming for simplicity that all grains have the same radius; (a)  $a = 0.03 \mu\text{m}$ , (b)  $a = 0.1 \mu\text{m}$  (fiducial model), (c)  $a = 0.3 \mu\text{m}$ , and (d)  $a = 1 \mu\text{m}$ . The relative number density of dust grains  $n_g/n_H$  is proportional to  $a^{-3}$  and is, for example,  $3.3 \times 10^{-11}$  and  $8.9 \times 10^{-13}$  for  $a = 0.03$  and  $0.1 \mu\text{m}$ , respectively. The results for a disk of  $f_\Sigma = 1$  and  $f_g = 1$  around a star of  $M_* = 1 M_\odot$  are shown in Figure 12. The other parameters are the same as in the fiducial model.

We find that the dead zone shrinks as the grain size increases. As the grains grow, the ion density increases because the total surface area of grains decreases and thus the recombination rate on grain surface decreases. For the case of  $\beta_c = 100$ , the critical radius  $r_{\text{crit}}$  is 37, 19, 7.6, and 4.6 AU for the models with  $a = 0.03, 0.1, 0.3,$  and  $1 \mu\text{m}$ , respectively.

For the case of  $a = 0.03 \mu\text{m}$ , the number density of dust grains becomes comparable to or higher than that of metal ions at  $n_H \gtrsim 10^8 \text{ cm}^{-3}$ . At the critical radius  $r_{\text{crit}} \approx 37$  AU on the midplane, the abundance of metal ions  $x(\text{M}^+) \approx 1.4 \times 10^{-12}$  is comparable to those of charged grains with  $\pm e$ , though the conductivity  $\sigma_c$  is still mainly contributed by electrons with abundance  $x(e) \approx 0.9 \times 10^{-14}$ .

So far we have assumed that all grains have the same radius. However, interstellar grains have a wide size distribution such as the MRN distribution for graphite and silicate grains,

$$\frac{dn_g}{da} = A n_H a^{-3.5}, \quad a_{\text{min}} < a < a_{\text{max}}, \quad (26)$$

where  $a_{\text{min}} \approx 0.005 \mu\text{m}$ ,  $a_{\text{max}} \approx 0.25 \mu\text{m}$ , and  $A \approx 1.5 \times 10^{-25} \text{ cm}^{2.5}$  (Draine & Lee 1984). For comparison, we show the results for this size distribution. Figure 13 shows the vertical distribution of the relative abundances  $n(\text{X})/n_H$  of some representative particles at 1 AU.

The qualitative features are essentially the same as those for the fiducial model (see Fig. 4). The total surface area of grains is contributed mainly by grains with radius  $a \approx a_{\text{min}}$  in the MRN distribution. Therefore, decrease of  $a_{\text{min}}$  enhances the recombination rate of ions and electrons on grains;  $a_{\text{min}}$  can be smaller than  $0.005 \mu\text{m}$  (MRN). Dust grains with electric charge  $\pm e$  are the dominant charged particles at the midplane everywhere within  $r \approx 100$  AU. In this case the magnetic field dissipation is more effective than in the fiducial model. The magnetorotational instability is suppressed in a wider region, and the critical radii on the midplane  $r_{\text{crit}} = 44$  and 59 AU for the cases of  $\beta_c = 100$  and 1000, respectively, are 2 to 3 times larger than those for the fiducial model.

## 4. DISCUSSION

#### 4.1. Layered Accretion

In paper I we have found that, in some disk conditions, the unstable modes have large amplitudes localized at the upper layer of the disk. This implies that the magnetorotational instability in the nonlinear regime enables the angular momentum transport only in this layer, and thus the layered accretion occurs as proposed by Gammie (1996). This layer corresponds to the unstable region at  $r \lesssim r_{\text{crit}}$  shown by the stripes in Figure 7. Since this unstable layer locates at a height a few times the scale height of the disk, the column density of this layer is very small. Therefore, the layered accretion might hardly affect dynamical evolution of the disks. However, the thickness of this layer is determined by the distribution of the magnetic diffusivity, which depends not only on the density distribution but also on the size and abundance of grains.

First, we examine the dependence of the column density of the unstable layer,  $\Sigma_{\text{uns}}$ , on the depletion factor of dust grains,  $f_g$ . Because the column density of the layer above the critical curve  $\lambda_{\text{ideal}}/H = 1$  is quite small, we approximate  $\Sigma_{\text{uns}}$  as the total column density of the disk subtracted by the column density of the dead zone. Figure 14a shows  $\Sigma_{\text{uns}}$  as a function of  $r$  for  $\beta = 100$  for three cases of grain depletion,  $f_g = 1, 10^{-2},$  and  $10^{-4}$ . The grain size is taken to be  $a = 0.1 \mu\text{m}$  and the other parameters are the same as in the fiducial model. The column density  $\Sigma_{\text{uns}}$  increases as the grain fraction decreases. Gammie (1996) assumed that the column density of the unstable region was comparable to the attenuation length  $\chi_{\text{CR}} \approx 96 \text{ g cm}^{-2}$ . We have found that the column density  $\Sigma_{\text{uns}}$  is much smaller than  $\chi_{\text{CR}}$  unless  $f_g \lesssim 10^{-4}$ . Magnetic fields can be decoupled from the gas even when cosmic rays are not attenuated.

Next we examine the dependence of  $\Sigma_{\text{uns}}$  on the grain size. Figure 14b shows the column density  $\Sigma_{\text{uns}}$  for the models with  $a = 0.1, 0.3,$  and  $1 \mu\text{m}$ . Here we have assumed the grain fraction  $f_g = 1$  and  $\beta_c = 100$ . The column density  $\Sigma_{\text{uns}}$  increases as the grain radius increases. However,  $\Sigma_{\text{uns}}$  is at most a few  $\text{g cm}^{-2}$  within  $r \sim 1 \text{ AU}$ , even when the grain is as large as  $a = 1 \mu\text{m}$ . Therefore, unless the abundance of dust grains is reduced to  $10^{-4}$  times the interstellar abundance, mass accretion through the unstable layer above the dead zone is very faint and the matter must accumulate around the outer boundary of the dead zone.

#### 4.2. Mass Accretion Rate

We estimate the mass accumulation rate into the dead zone. Sano, Inutsuka, & Miyama (1998) investigated the nonlinear evolution of magnetorotational instability including the effect of ohmic dissipation using two-dimensional MHD simulations. Their results show that, at the saturated turbulent state, the efficiency of angular momentum transport depends on the strength of the initial magnetic field perpendicular to the disk, and that when the magnetic Reynolds number  $R_m \equiv v_A^2/\eta\Omega$  is around unity, the  $\alpha$  parameter of the viscosity (Shakura & Sunyaev 1973) is given by

$$\alpha \approx 1.8 \times 10^{-2} \left( \frac{\beta}{1000} \right)^{-1}, \quad (27)$$

where  $\beta$  is the plasma beta for the initial field.



Because the magnetic Reynolds number  $R_m$  is close to unity around the critical radius, the mass accretion rate can be estimated with equation (27). The radial accretion velocity  $v_r$  is given by  $v_r \sim \nu/r$ , where  $\nu = \alpha c_s H$  is the kinematic viscosity. Then the mass accretion rate at  $r \approx r_{\text{crit}}$  is given by

$$\dot{M} \sim 2\pi r_{\text{crit}} \Sigma v_r \approx 4.9 \times 10^{-7} f_\Sigma \left( \frac{r_{\text{crit}}}{19 \text{ AU}} \right)^{-1/2} \left( \frac{\beta_c}{100} \right)^{-1} M_\odot \text{ yr}^{-1}, \quad (28)$$

for the disks whose structure is given by equations (3), (5), and (7) with  $q = 3/2$  and  $M_* = 1 M_\odot$ . For the case of  $\beta_c = 1000$ , the mass accretion rate at  $r \approx r_{\text{crit}} \approx 22 \text{ AU}$  is an order of magnitude smaller.

The typical age of T Tauri stars is estimated to be  $10^6 \text{ yr}$  (Kenyon & Hartmann 1995), and the lifetime of protoplanetary disks must be comparable to or longer than the age of T Tauri stars. If mass accretion with a rate  $\dot{M} \sim 10^{-6} M_\odot \text{ yr}^{-1}$  continues and the accreted matter is distributed relatively widely inside  $r \approx r_{\text{crit}}$ , the disk of this part becomes gravitationally unstable at some stage, and the resultant gravitational torque causes mass accretion in this region. This makes the accretion onto the central star non-steady. If the accreting matter accumulates near the critical radius  $r \approx r_{\text{crit}}$  and a dense ring forms, a planet or a brown dwarf would be formed due to fragmentation of the ring (Nakano 1991). In this case, the critical radius gives the position where the first small companion forms.

Higher mass disks have higher accretion rate as seen from equation (28). The mass accretion rate for a disk of  $f_\Sigma = 10$  at  $r \approx r_{\text{crit}} \approx 39 \text{ AU}$  is 7 times larger than that of the fiducial model at  $r_{\text{crit}} \approx 19 \text{ AU}$ . For the model of  $f_\Sigma = 0.3$ , we have the mass accretion rate  $\dot{M} \sim 1.8 \times 10^{-7} M_\odot \text{ yr}^{-1}$  at  $r \approx r_{\text{crit}} \approx 13 \text{ AU}$ . Therefore, higher mass disks become gravitationally unstable in shorter time scale.

### 4.3. Evolution of Dust Grains in Protoplanetary Disks

Investigating the growth and sedimentation of dust grains in protoplanetary disks, Nakagawa et al. (1981) showed that dust grains can grow by sticking through mutual collisions in thermal Brownian motion, e.g., when the grain size is smaller than microns at  $r \approx 1 \text{ AU}$ . The collision time in Brownian motion,  $t_{\text{col}}$ , is given by

$$t_{\text{col}} = 2\pi \frac{(\rho_g/3)^{3/2} \bar{a}^{5/2}}{\zeta_g \rho (kT)^{1/2}} = 21 \left( \frac{\rho_g}{3 \text{ g cm}^{-3}} \right)^{3/2} \left( \frac{\bar{a}}{1 \mu\text{m}} \right)^{5/2} \left( \frac{\zeta_g}{0.0034} \right)^{-1} \left( \frac{r}{1 \text{ AU}} \right)^{3/2} t_K, \quad (29)$$

where  $\rho_g$  and  $\bar{a}$  are the internal density and the mean radius, respectively, of dust grains, and  $\zeta_g$  is the mass fraction of dust grains, and the last expression is at the midplane of the fiducial model. As seen from equation (29), dust grains in dense regions grow to micron size in a time comparable to the dynamical time scale,  $t_K$ , and much shorter than the time scale of sedimentation,

$$t_{\text{sed}} = \frac{1}{2\pi} \frac{\rho H}{\rho_g \bar{a}} t_K = 5.2 \times 10^5 \left( \frac{\rho_g}{3 \text{ g cm}^{-3}} \right)^{-1} \left( \frac{\bar{a}}{1 \mu\text{m}} \right)^{-1} \text{ yr}, \quad (30)$$

where the last expression is at the midplane of the fiducial model and is independent of  $r$ .

Numerical calculations of Nakagawa et al. (1981) show that the mass fraction of floating grains,  $f_g$ , at  $r = 1$  AU is  $\sim 10^{-1}$ ,  $10^{-2}$ , and  $10^{-4}$  at the time  $t \sim 2 \times 10^3$ ,  $10^4$ , and  $10^5$  yr, respectively, and that the size of floating grains,  $a$ , is  $1 - 10 \mu\text{m}$  in the late stages. Although laminar flow was assumed in their analysis, we discuss the evolution of the unstable regions using their results. Figure 12d shows the unstable region for the model with  $a = 1 \mu\text{m}$ , an order of magnitude larger than in the fiducial model. The critical radius on the midplane  $r_{\text{crit}}$  is 4.6 and 5.8 AU for the cases of  $\beta_c = 100$  and 1000, respectively. The dead zone shrinks as the sedimentation of dust grains proceeds; in the cases of  $f_g = 10^{-1}$ ,  $f_g = 10^{-2}$ , and  $f_g = 10^{-4}$ , the critical radius of the models with  $a = 1 \mu\text{m}$  is 3.2 (3.8), 2.3 (2.7), and 1.4 (1.6) AU, respectively, for  $\beta_c = 100$  (1000). In all these cases the critical radius  $r_{\text{crit}}$  is less than 6 AU. If dust grains in protoplanetary disks could grow to micron size, most parts of the disk become magnetorotationally unstable. Therefore, sedimentation of dust grains must be prevented by turbulence induced by this instability contrary to the assumption of Nakagawa et al. (1981).

According to the standard scenario of solar system formation (Hayashi et al. 1985), planets form by accretion of planetesimals, which are produced through gravitational instability of a thin dust layer (Goldreich & Ward 1973). The thin layer is formed by sedimentation of dust, which must occur only in a quiescent disk (Mizuno, Markiewicz, & Völk 1988). By sedimentation the disk becomes magnetorotationally unstable and turbulent, preventing sedimentation as shown in §3.3. Therefore we have to investigate the gas motion and the evolution of dust simultaneously.

#### 4.4. Ionization by X-Rays

So far we have considered only cosmic rays and radioactive elements as the ionization sources of protoplanetary disks. In this subsection we consider the effect of photo-processes. The protoplanetary disks are exposed to the UV radiation from the central star and from the interstellar space. Because of the very small attenuation length, a few  $\times 10^{-3} \text{ g cm}^{-2}$ , the ionization by UV radiation is inefficient except for very thin surface layers.

Young stellar objects are strong X-ray sources (e.g., Glassgold, Feigelson, & Montmerle 2000). The X-ray luminosity of low-mass young stellar objects is typically in the range  $L_X \sim 10^{28} - 10^{30} \text{ erg s}^{-1}$ , or a factor of  $10^2 - 10^3$  above the contemporary solar levels. Some X-ray sources exhibit high-amplitude rapid flares with peak luminosity  $L_X \sim 10^{30} - 10^{32} \text{ erg s}^{-1}$ . These emissions require the presence of a large volume of high-density plasma at a temperature of about  $10^7 \text{ K}$ . The plasma must be magnetically confined, probably in large loops on a scale comparable to or larger than the X-ray emitting star itself. Field lines linking the star with the disk at the corotating radius may explain the strongest of these powerful flares (Shu et al. 1994; Hayashi, Shibata, & Matsumoto 1996). The X-rays can induce a wide variety of changes in chemical and physical properties of protoplanetary disks.

Soft X-rays can be the most promising ionization sources for protoplanetary disks as well as cosmic rays. While the underlying ionization mechanism is due to electronic collisions in both cases, X-rays are absorbed in a smaller column of matter than cosmic rays. Thus cosmic rays provide a more global, low-level ionization of the disks, whereas X-rays can produce a localized

high-level ionization.

Igea & Glassgold (1999) investigated the X-ray transfer and ionization in the disks around young stellar objects using a Monte Carlo method. The X-ray emitting region was modeled as a ring of radius  $r = 10 R_{\odot}$  at height  $z = 10 R_{\odot}$  with  $L_X = 10^{29} \text{ erg s}^{-1}$  based on the x-wind model of Shu et al. (1994). They obtained the ionization rates at 1 – 10 AU of the minimum-mass solar nebula as functions of the vertical column density into the disk by hydrogen number,  $N_{\perp}$ . Their results show that the ionization rate by X-rays is larger than that by cosmic rays,  $\zeta_{\text{CR}} \approx 10^{-17} \text{ s}^{-1}$ , only at  $N_{\perp}$  smaller than  $10^{25}$  to  $2 \times 10^{23} \text{ cm}^{-2}$  depending on  $r$ , which is much smaller than the total column density of the disk at each  $r$ . Therefore, most of our results are preserved even if X-ray ionization is taken into account. For instance, the thickness of the dead zone is hardly affected by the X-ray ionization. Even if cosmic rays are excluded from the inner regions of protoplanetary disks by, e.g., stellar winds (Parker 1960), the active surface layer can be maintained by the X-ray ionization (Igea & Glassgold 1999). Igea & Glassgold (1999) neglected the effects of dust grains on ion densities and on interaction with magnetic fields. However, the column densities of unstable regions  $\Sigma_{\text{uns}}$  must be affected by the characters of dust grains in the disk in the same way as in the cases with the cosmic ray ionization investigated in §3.

#### 4.5. Uncertainties in the Disk Temperature

The temperature distribution given by equation (4) with  $p = 1/2$  holds for the disk transparent to the radiation from the central star. Actually, the inner dense regions of protoplanetary disks would be optically thick and there would be some other heating sources such as viscous heating and dissipation of magnetic fields. However, the results are not very sensitive to the temperature as long as it is below several hundred Kelvin where the thermal ionization is inefficient. Figure 15 shows the column densities of the unstable layers for the models with temperature ten times higher (dashed curve) and ten times lower (dot-dashed curve) than the fiducial model (solid curve). The other parameters are the same as those of the fiducial model. The difference in  $\Sigma_{\text{uns}}$  is surprisingly small for such large changes in the temperature. We also investigated for  $p = 0$  and  $3/4$ , and obtained quite similar results assuming as above that the thermal ionization is inefficient. When the temperature is higher than several hundred Kelvin, the thermal ionization becomes efficient and there would be significant effects on the instability. This would happen only in the innermost region  $r \lesssim 0.1 \text{ AU}$  for the minimum-mass model, which is much smaller than the dead zones obtained in this paper. Notice that the temperature of steady accretion disks ( $p = 3/4$ ) with typical mass accretion rate is within the range we examined here.

#### 4.6. Validity of Ionization-Recombination Equilibrium

We have used the densities of charged particles obtained by assuming that the gas is in ionization-recombination equilibrium. This assumption is valid when the relaxation time to an equilibrium state for each kind of charged particles is much shorter than the characteristic time scale of protoplanetary disks. The relaxation time  $t_{\text{r}}(X_i)$  to the ionization-recombination

equilibrium for a species  $X_i$  is approximately given by the minimum of

$$\left| \frac{n(X_i)}{\beta_{ijk}n(X_j)n(X_k)} \right|. \quad (31)$$

We estimate  $t_r(X_i)$  by using the equilibrium abundances of particles adopted in the previous section. Figure 16a shows the time scales near the midplane as functions of  $r$ , and Figure 16b shows those in the Earth’s region ( $r = 1$  AU) as functions of  $|z|$ , for the fiducial model.

As seen from Figure 16a, the gas near the midplane is almost in ionization-recombination equilibrium at  $r \gtrsim 1.3$  AU because  $t_r$  is smaller than  $t_K$  for all the particles. At  $r \lesssim 1$  AU, however,  $t_r$  for neutral grains is much longer than  $t_K$ . Because  $t_r$  for ions and electrons is much shorter than  $t_r$  for grains, ions and electrons always take quasi-equilibrium abundances determined for the temporary charge-state distribution of grains. When the charge-state distribution deviates significantly from the equilibrium, the relaxation time to its true equilibrium is about 250 yr, much longer than  $t_K$  (see Fig 16a). However, because this is much shorter than the sedimentation time of grains in this region of the solar nebula (Nakagawa et al. 1981), the ionization-recombination equilibrium can be attained even in this region.

In Earth’s region the time scale  $t_r$  for metal ions and electrons is longer than  $t_K$  only at  $|z| \gtrsim 3.7 H$  as seen from Figure 16b. Because most of the disk matter is inside this layer, a possible deviation from the ionization-recombination equilibrium hardly affects the results obtained in the previous sections and subsections.

As the depletion factor  $f_g$  of dust grains decreases, the time scale  $t_r$  for dust grains decreases considerably in regions where ions and electrons are the dominant charged particles. For ions and electrons  $t_r$  remains at least 10 times smaller than  $t_K$  even at such late evolutionary stages as  $f_g = 10^{-4}$ . In the inner regions where dust grains are the dominant charged particles,  $t_r$  for dust grains increases extensively as  $r$  decreases, and it finally exceeds  $t_K$  at a certain position. For the case of  $f_g = 10^{-4}$  the time scale  $t_r$  for charged grains exceeds  $t_K$  only at  $r \lesssim 0.66$  AU, and its value is at most 300 times longer than  $t_K$  even in the innermost region  $r \lesssim 0.5$  AU. Because the evolutionary time scale of the protoplanetary disk is much longer than  $t_K$ , we can regard that the solar nebula is in ionization-recombination equilibrium even at stages of  $f_g \approx 10^{-4}$  except at high  $|z|$  where little matter exists. The situation is qualitatively the same for the other disks investigated in the previous section.

## 5. SUMMARY

We have investigated the ionization state and magnetorotational instability for various models of protoplanetary disks taking the effect of charged grains into account. Our findings are summarized as follows.

1. In early evolutionary stages of the minimum-mass solar nebula, we have found that magnetorotational instability operates outside the critical radius  $r_{\text{crit}} \approx 20$  AU. Inside the critical radius most part of the disk is stabilized by ohmic dissipation. Thus, the accreting

matter accumulates near the critical radius unless some other mechanisms of angular momentum transport are effective.

2. Just outside this critical radius, the mass accretion rate is  $10^{-7} - 10^{-6} M_{\odot} \text{ yr}^{-1}$ . By accumulation of matter at this rate the inner region becomes gravitationally unstable within the typical lifetime of protoplanetary disks. This suggests that non-steady accretion onto the central star occurs as in FU Orionis objects.
3. The critical radius  $r_{\text{crit}}$  depends on the mass of the disk. Because the abundances of charged particles are lower in denser regions, the disks of higher mass have larger stable regions and thus larger  $r_{\text{crit}}$ .
4. As dust grains in the disk grow or sediment toward the equatorial plane, the critical radius  $r_{\text{crit}}$  decreases. This suggests that magnetorotational instability is important in late evolutionary stages of the disks exciting turbulence and suppressing sedimentation of dust grains. Therefore, to clarify the processes of planet formation, behavior of grains should be studied in connection with gas motion.
5. Even in the inner regions  $r \lesssim r_{\text{crit}}$ , some part of the surface layer is magnetorotationally unstable. However, because the column density of this layer is so low unless the grain fraction is as low as  $f_{\text{g}} \lesssim 10^{-4}$  that the layered accretion must not be effective at least in the early evolutionary stages.

Numerical computations were partly carried out at the Astronomical Data Analysis Center of the National Astronomical Observatory, Japan. This work was partly supported by Grant-in-Aid for Scientific Research on Priority Areas (10147105) of the Ministry of Education, Science, Sports, and Culture of Japan.

### A. MOMENTUM TRANSFER RATE BETWEEN ELECTRONS AND NEUTRAL PARTICLES

M. Hayashi (1981) compiled the values of the momentum transfer cross sections of an electron in collision with a hydrogen molecule and a helium atom at low energies, which are not much different from the geometrical cross sections and are significantly smaller than the Langevin's values. From these values we have obtained the empirical formulae for the momentum transfer rate coefficients as functions of the temperature  $T$  as follows,

$$\langle \sigma v \rangle_{\text{e-H}^2} \approx \left( \frac{8kT}{\pi m} \right)^{1/2} \left[ 7.94 \times 10^{-16} - 2.52 \times 10^{-16} \log T + 1.19 \times 10^{-16} (\log T)^2 \right], \quad (\text{A1})$$

$$\langle \sigma v \rangle_{\text{e-He}} \approx \left( \frac{8kT}{\pi m} \right)^{1/2} \left[ 5.30 \times 10^{-16} - 4.70 \times 10^{-16} \log T + 2.31 \times 10^{-16} (\log T)^2 \right], \quad (\text{A2})$$

where  $m$  is the reduced mass.

Equations (A1) and (A2) give the rate coefficients about two orders of magnitude smaller than those used previously by many authors. Thus, we find that electrons are much more tightly coupled with magnetic field than previously considered.

## REFERENCES

- Adams, F. C., Lada, C. J., & Shu, F. H. 1987, *ApJ*, 312, 788
- Adams, F. C., Lada, C. J., & Shu, F. H. 1988, *ApJ*, 326, 865
- Anders, E., & Grevesse, N. 1989, *Geochim. Cosmochim. Acta*, 53, 197
- Balbus, S. A., & Hawley, J. F. 1991, *ApJ*, 376, 214
- Balbus, S. A., & Hawley, J. F. 1998, *Rev. Mod. Phys.*, 70, 1
- Beckwith, S. V. W., Sargent, A. I., Chini, R. S., & Güsten, R. 1990, *AJ*, 99, 924
- Bertout, C., Basri, G., & Bouvier, J. 1988, *ApJ*, 330, 350
- Blaes, O. M., & Balbus, S. A. 1994, *ApJ*, 421, 163
- Cassen, P. 1994, *Icarus*, 112, 429
- Draine, B. T., & Lee, H. M. 1984, *ApJ*, 285, 89
- Draine, B. T., & Sutin, B. 1987, *ApJ*, 320, 803
- Gammie, C. F. 1996, *ApJ*, 457, 355
- Glassgold, A. E., Feigelson, E. D., & Montmerle, T. 2000, in *Protostars & Planets IV*, ed. V. G. Mannings, A. P. Boss, & S. Russell (Tuscon: Univ. of Arizona Press), in press
- Glassgold, A. E., Najita, J., & Igea, J. 1997, *ApJ*, 480, 344
- Goldreich, P., & Lynden-Bell, D. 1965, *MNRAS*, 130, 97
- Goldreich, P., & Ward, W. R. 1973, *ApJ*, 183, 1051
- Hayashi, C. 1981, *Prog. Theor. Phys. Suppl.*, No. 70, 35
- Hayashi, C., Nakazawa, K., & Nakagawa, Y. 1985, in *Protostars & Planets II*, ed. D. C. Black & M. S. Matthews (Tuscon: Univ. of Arizona Press), 1100
- Hayashi, M. 1981, IPPJ-AM-19 (IPP/Nagoya Univ., Nagoya)
- Hayashi, M. R., Shibata, K., & Matsumoto, R. 1996, *ApJ*, 468, L37
- Igea, J., & Glassgold, A. E. 1999, *ApJ*, 518, 848
- Jin, L. 1996, *ApJ*, 457, 798

- Kenyon, S. J., & Hartmann, L. 1995, *ApJS*, 101, 117
- Lynden-Bell, D., & Pringle, J. E. 1974, *MNRAS*, 168, 603
- Marcy, G. W., Cochran, W. D., & Mayor, M. 2000, in *Protostars & Planets IV*, ed. V. G. Mannings, A. P. Boss, & S. Russell (Tucson: Univ. of Arizona Press), in press
- Mathis, J. S., Rumpl, W., & Nordsieck, K. H. 1977, *ApJ*, 217, 425 (MRN)
- Millar, T. J., Farquhar, P. R. A., & Willacy, K. 1997, *A&AS*, 121, 139
- Mitchell, G. F., Kuntz, P. J., & Ginsburg, J. L. 1978, *ApJS*, 38, 39
- Mizuno, H., Markiewicz, W. J., & Völk, H. J. 1988, *A&A*, 195, 183
- Nakagawa, Y., Nakazawa, K., & Hayashi, C. 1981, *Icarus*, 45, 517
- Nakano, T. 1984, *Fundam. Cosmic Phys.*, 9, 139
- Nakano, T. 1991, *Mem. Soc. Astron. Ital.*, 62, 841
- Nakano, T., & Umebayashi, T. 1988, *Prog. Theor. Phys. Suppl.*, No. 96, 73
- Nishi, R., Nakano, T., & Umebayashi, T. 1991, *ApJ*, 368, 181
- Osterbrock, D. E. 1961, *ApJ*, 134, 270
- Parker, E. N. 1960, *ApJ*, 132, 821
- Rucinski, S. M. 1985, *AJ*, 90, 2321
- Sano, T., Inutsuka, S., & Miyama, S. M. 1998, *ApJ*, 506, L57
- Sano, T., & Miyama, S. M. 1999, *ApJ*, 515, 776 (Paper I)
- Shakura, N. I., & Sunyaev, R. A. 1973, *A&A*, 24, 337
- Shu, F., Najita, J., Ostriker, E., Wilkin, F., Ruden, S., & Lizano, S. 1994, *ApJ*, 429, 781
- Umebayashi, T. 1983, *Prog. Theor. Phys.*, 69, 480
- Umebayashi, T., & Nakano, T. 1980, *PASJ*, 32, 405
- Umebayashi, T., & Nakano, T. 1981, *PASJ*, 33, 617
- Umebayashi, T., & Nakano, T. 1988, *Prog. Theor. Phys. Suppl.*, No. 96, 151
- Umebayashi, T., & Nakano, T. 1990, *MNRAS*, 243, 103

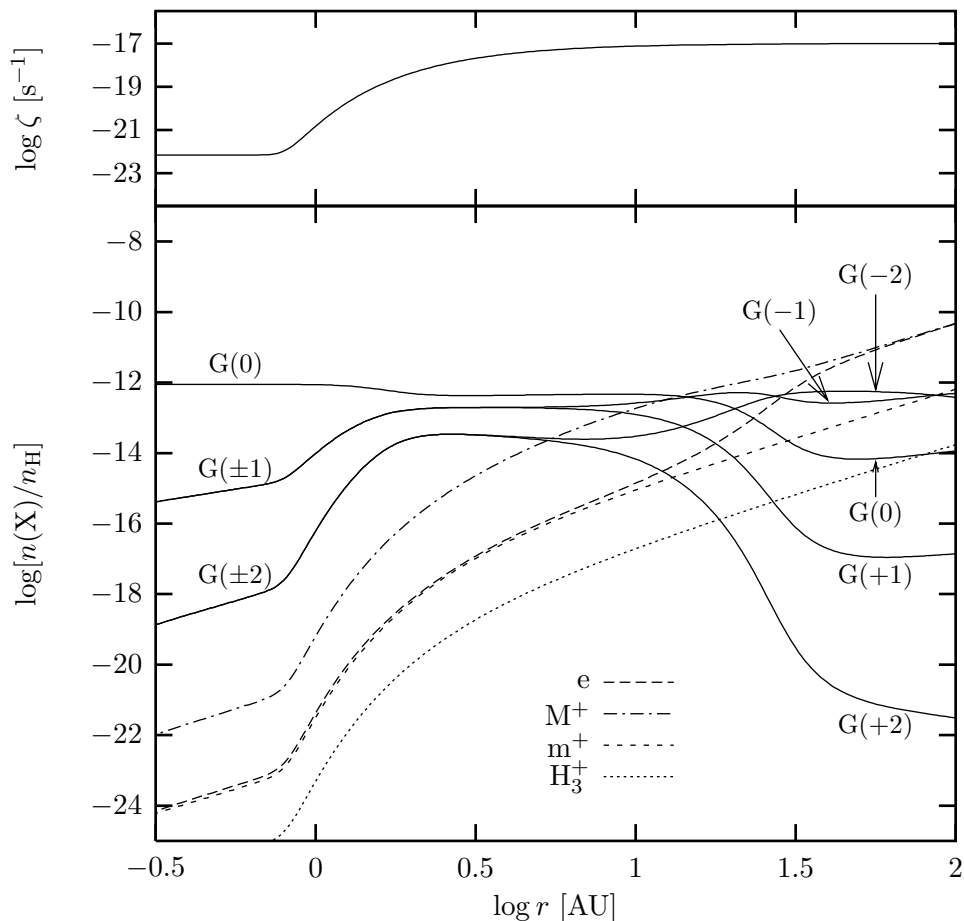


Fig. 1.— Relative abundances  $n(X)/n_H$  (*lower panel*) of some representative particles on the midplane of a disk with  $q = 3/2$ ,  $f_\Sigma = 1$ ,  $p = 1/2$ ,  $T_0 = 280$  K,  $M_* = 1 M_\odot$ , and  $f_g = 1$  as functions of the distance  $r$  from the star. We call this the fiducial model because it is expected to well represent the primitive solar nebula in an early evolutionary stage. We adopted the depletion factors of heavy elements from the gas phase  $\delta_1 = 0.2$  and  $\delta_2 = 0.02$ , the fraction of gas phase oxygen in the form of  $O_2$ ,  $H_2O$ , or  $OH$   $f_{O_2} = 0.7$ , and the radius of dust grains  $a = 0.1 \mu\text{m}$ .  $G(n)$  represents grains with electric charge  $ne$ . The upper panel shows the ionization rate  $\zeta$  on the midplane as a function of  $r$ .



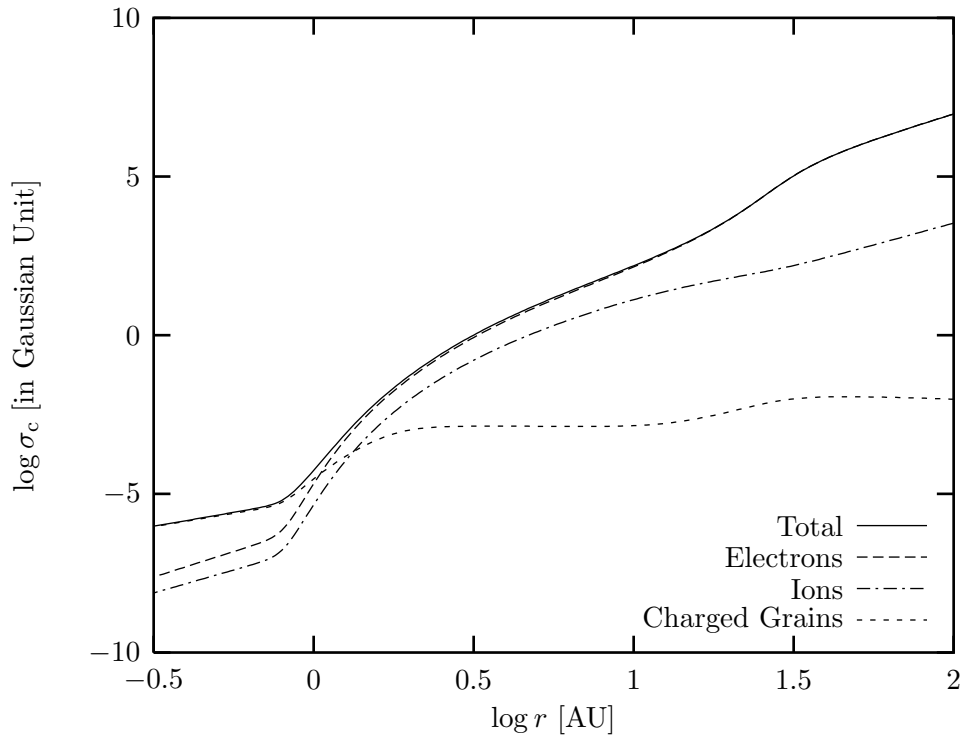


Fig. 2.— The electrical conductivity  $\sigma_c$  on the midplane of the fiducial model (same as in Fig. 1) as a function of the distance  $r$  from the star. Also shown are the contributions of electrons, ions, and charged grains to the conductivity.

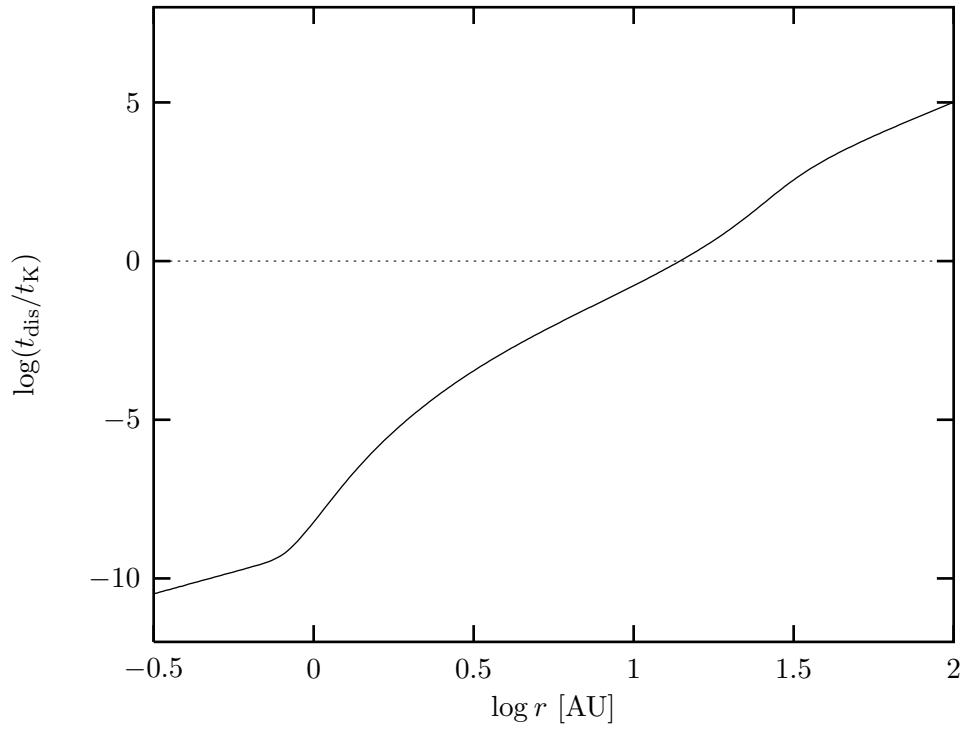


Fig. 3.— The ohmic dissipation time of magnetic field,  $t_{\text{dis}}$ , on the midplane relative to the Keplerian orbital period  $t_{\text{K}}$  as a function of  $r$  for the fiducial model. The magnetic diffusivity  $\eta$  given by equation (10) is evaluated with the abundances of charged particles shown in Figure 1.

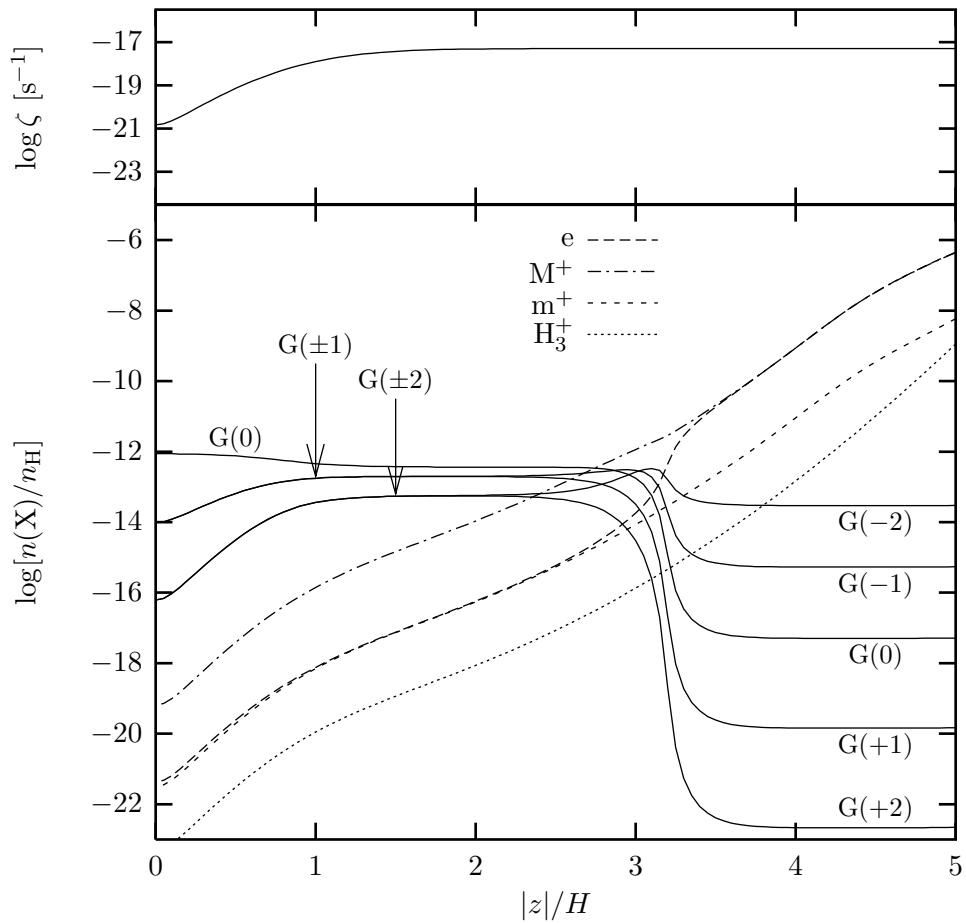


Fig. 4.— Relative abundances  $n(X)/n_H$  of some representative particles as functions of the height  $|z|$  from the midplane at  $r = 1$  AU for the same disk as in Figure 1. The upper panel shows the ionization rate  $\zeta$  as a function of  $|z|$ .

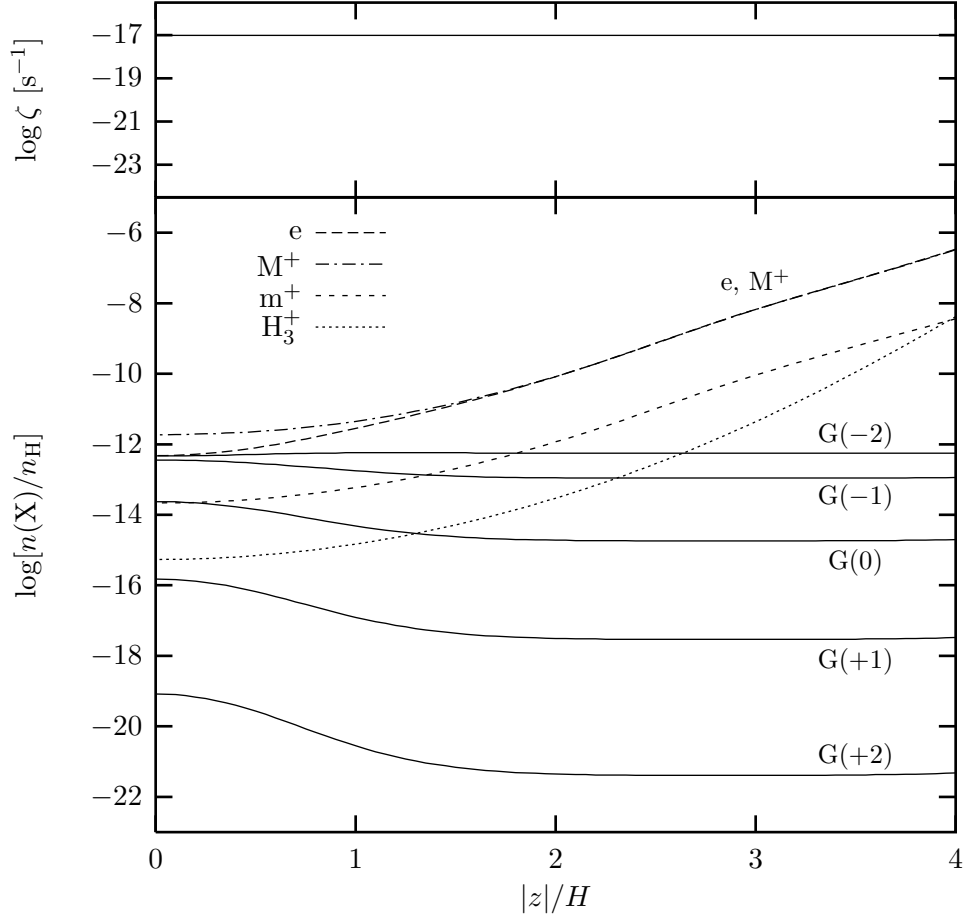


Fig. 5.— Relative abundances  $n(X)/n_H$  of some representative particles as functions of the height  $|z|$  from the midplane at  $r = 30$  AU for the same disk as in Figure 1. The upper panel shows the ionization rate  $\zeta$ .

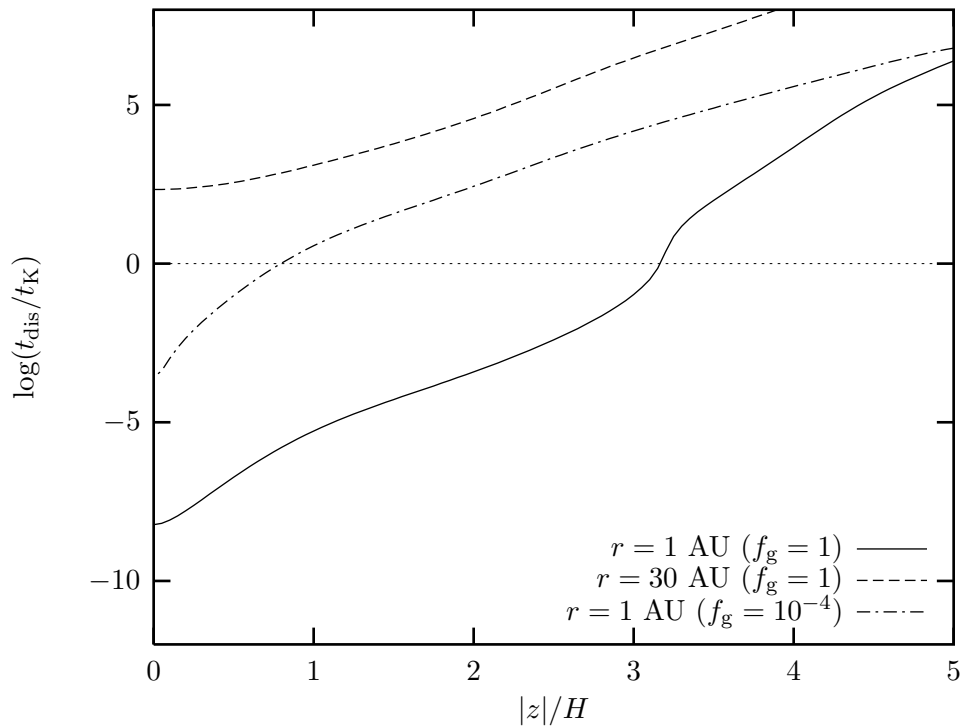


Fig. 6.— The ratio of the ohmic dissipation time  $t_{\text{dis}}$  to the Keplerian orbital period  $t_{\text{K}}$  as a function of  $|z|$  at  $r = 1 \text{ AU}$  (*solid curve*) and  $30 \text{ AU}$  (*dashed curve*). The magnetic diffusivity is evaluated with the abundances of charged particles shown in Figures 4 and 5 for the fiducial model. The dot-dashed curve is for the case of  $f_{\text{g}} = 10^{-4}$  at  $r = 1 \text{ AU}$ .

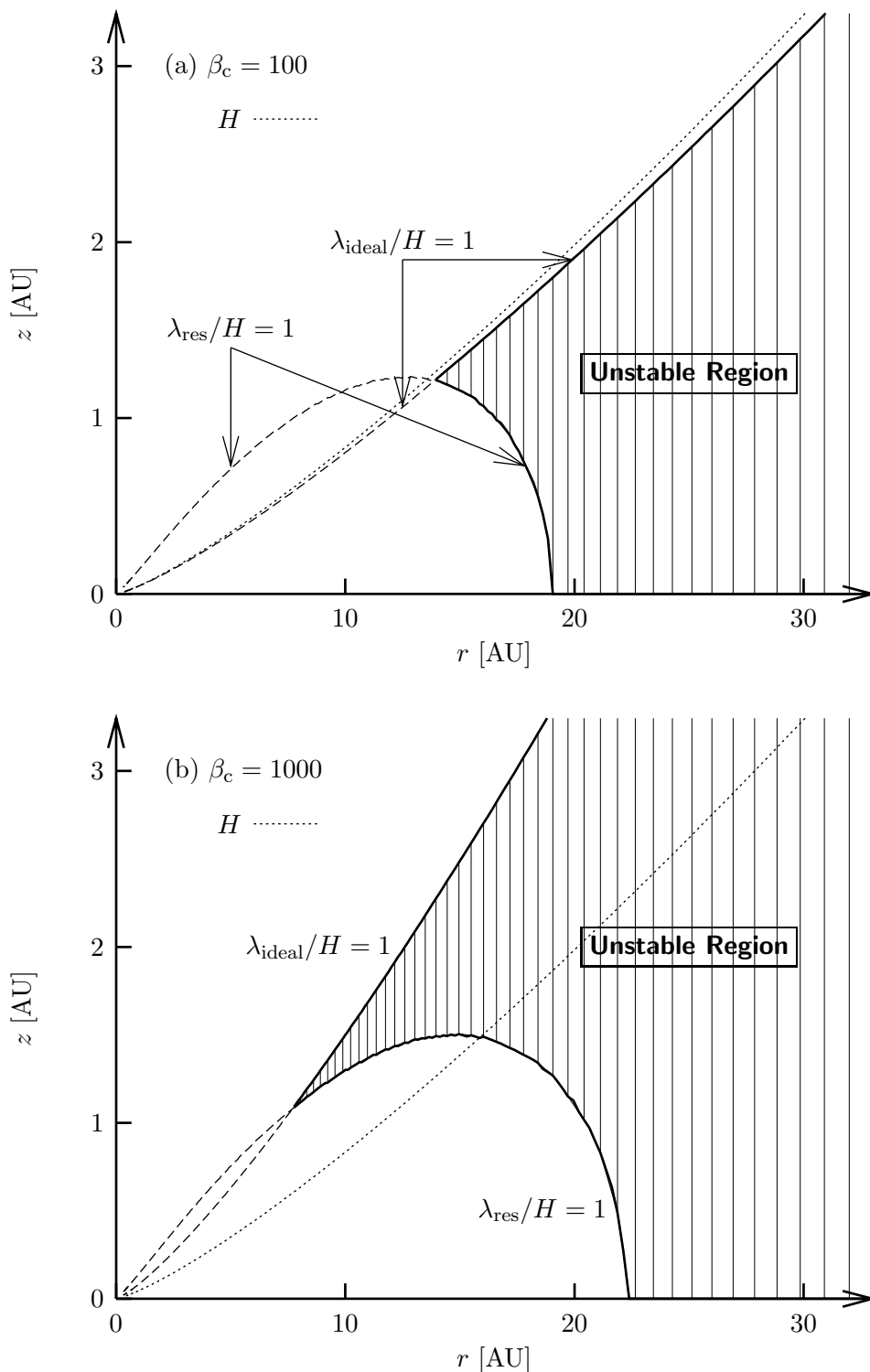


Fig. 7.— The unstable regions (*striped*) for the cases of (a) the plasma beta at the midplane  $\beta_c = 100$  and (b)  $\beta_c = 1000$  for the fiducial model (same as in Fig. 1). The dotted curve denotes the scale height of the disk,  $z = H(r)$ . In the region above the curve  $\lambda_{\text{ideal}}/H = 1$ , the instability does not effectively work because the wavelengths of the unstable modes are larger than the scale height of the disk. The region below the curve  $\lambda_{\text{res}}/H = 1$  is stable because the magnetic dissipation is effective, and corresponds to Gammie’s (1996) “dead zone”.

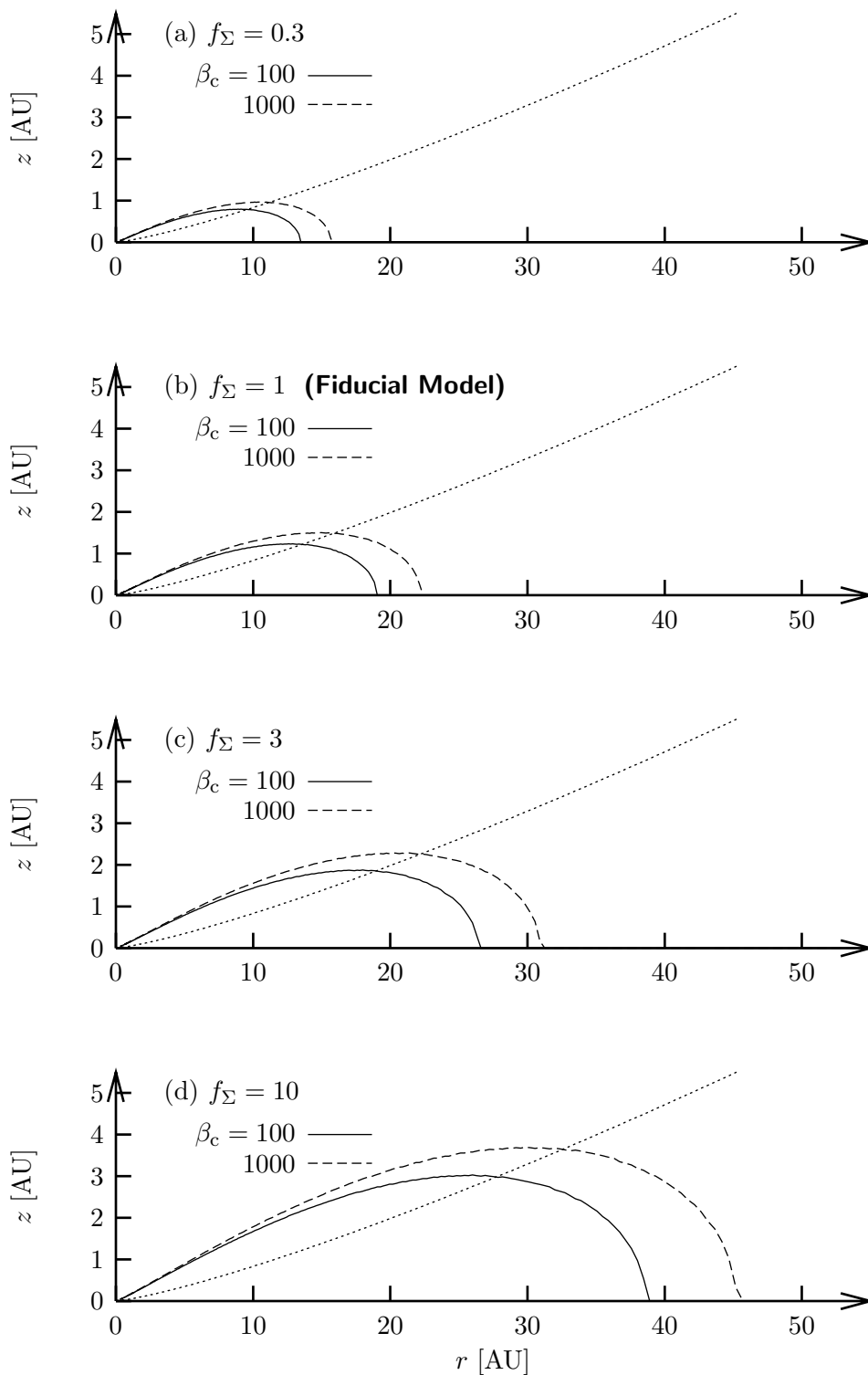


Fig. 8.— Unstable regions in the disks with various surface densities; (a)  $f_\Sigma = 0.3$ , (b)  $f_\Sigma = 1$  (the minimum-mass solar nebula), (c)  $f_\Sigma = 3$ , and (d)  $f_\Sigma = 10$ . The other parameters are the same as those of the fiducial model. The solid and dashed curves represent the loci of  $\lambda_{\text{res}}/H = 1$  for the cases of the field strength  $\beta_c = 100$  and 1000, respectively, inside of which is magnetorotationally stable. The dotted curve represents the scale height of the disk  $z = H(r)$ .

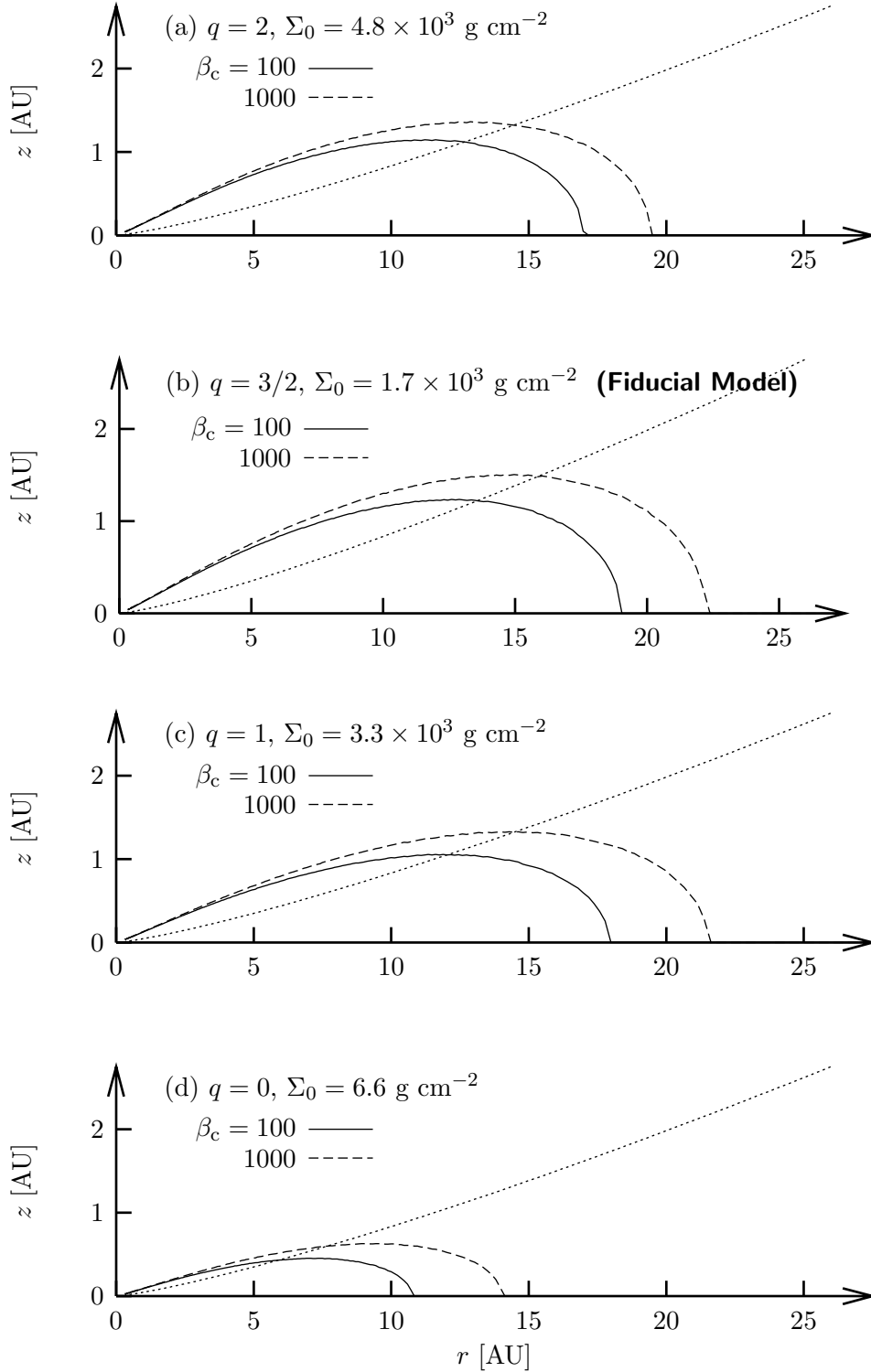


Fig. 9.— Unstable regions in the disks with various power indices for the surface density; (a)  $q = 2$ ,  $\Sigma_0 = 4.8 \times 10^3 \text{ g cm}^{-2}$ , (b)  $q = 3/2$ ,  $\Sigma_0 = 1.7 \times 10^3 \text{ g cm}^{-2}$ , (c)  $q = 1$ ,  $\Sigma_0 = 3.3 \times 10^2 \text{ g cm}^{-2}$ , and (d)  $q = 0$ ,  $\Sigma_0 = 6.6 \text{ g cm}^{-2}$ . The other parameters are the same as those of the fiducial model. All these models have the same disk mass  $0.024 M_\odot$  between 0.1 and 100 AU. The solid and dashed curves represent the loci of  $\lambda_{\text{res}}/H = 1$  for the cases of the field strength  $\beta_c = 100$  and 1000, respectively, inside of which is magnetorotationally stable. The dotted curve represents the scale height of the disk  $z = H(r)$ .



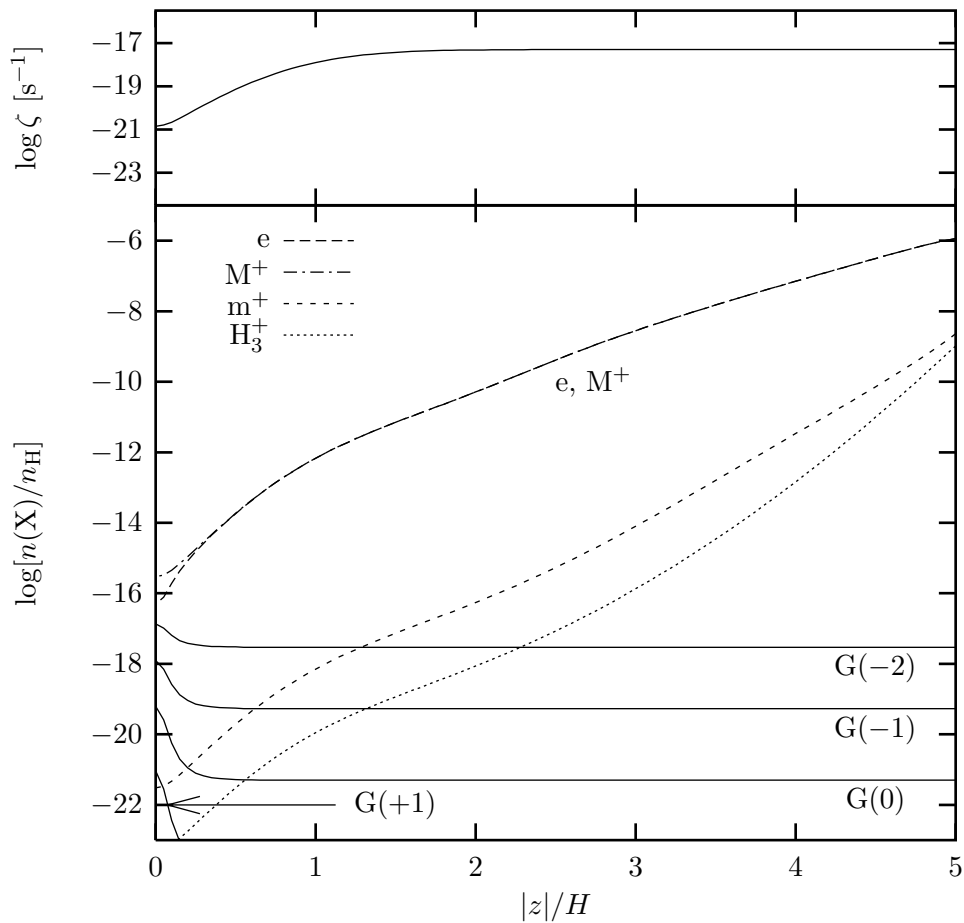


Fig. 10.— Relative abundances  $n(X)/n_H$  of some representative particles for the case of  $f_g = 10^{-4}$  as functions of the height  $|z|$  from the midplane at  $r = 1$  AU. The other parameters are the same as those of the fiducial model. The upper panel shows the ionization rate  $\zeta$ .

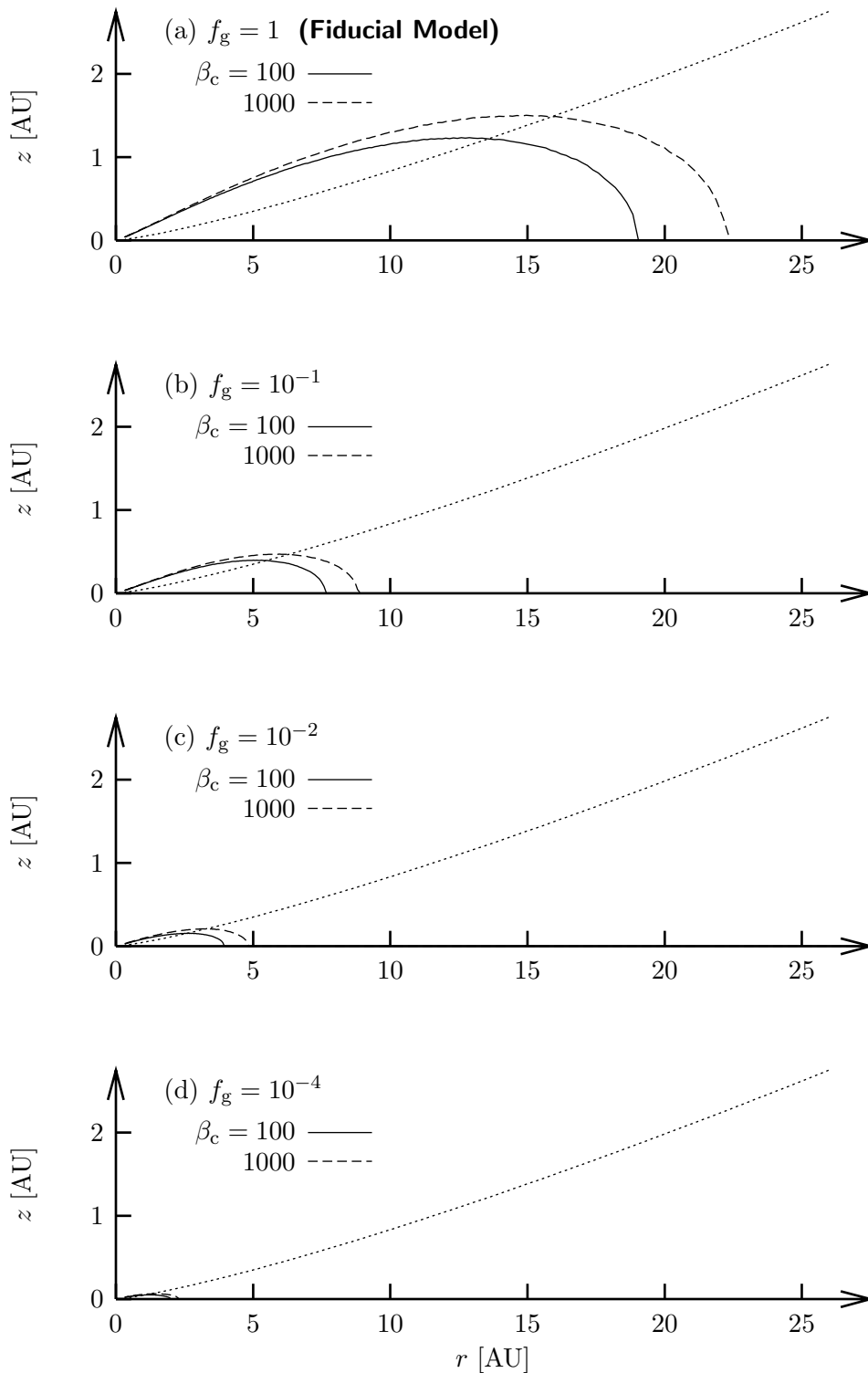


Fig. 11.— Unstable regions for the disk of various evolutionary stages; (a)  $f_g = 1$ , (b)  $f_g = 10^{-1}$ , (c)  $f_g = 10^{-2}$ , and (d)  $f_g = 10^{-4}$ . The other parameters are the same as those of the fiducial model. The solid and dashed curves represent the loci of  $\lambda_{\text{res}}/H = 1$  for the cases of the field strength  $\beta_c = 100$  and  $1000$ , respectively, inside of which is magnetorotationally stable. The dotted curve represents the scale height of the disk  $z = H(r)$ .

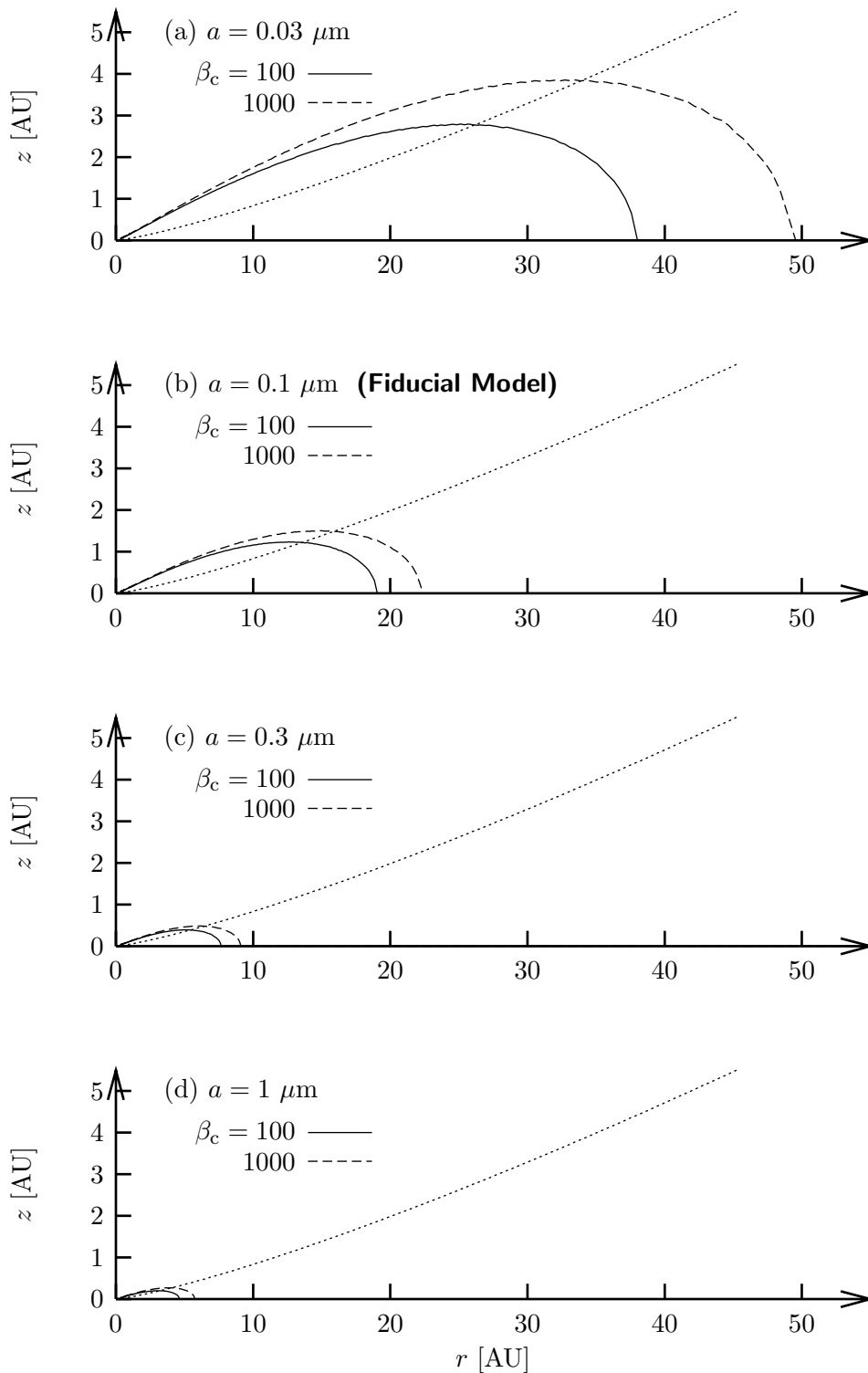


Fig. 12.— Unstable regions for the disks with various grain sizes; (a)  $a = 0.03 \mu\text{m}$ , (b)  $a = 0.1 \mu\text{m}$ , (c)  $a = 0.3 \mu\text{m}$ , and (d)  $a = 1 \mu\text{m}$ . The other parameters are the same as those of the fiducial model. The solid and dashed curves represent the loci of  $\lambda_{\text{res}}/H = 1$  for the cases of the field strength  $\beta_c = 100$  and  $1000$ , respectively, inside of which is magnetorotationally stable. The dotted curve represents the scale height of the disk  $z = H(r)$ .

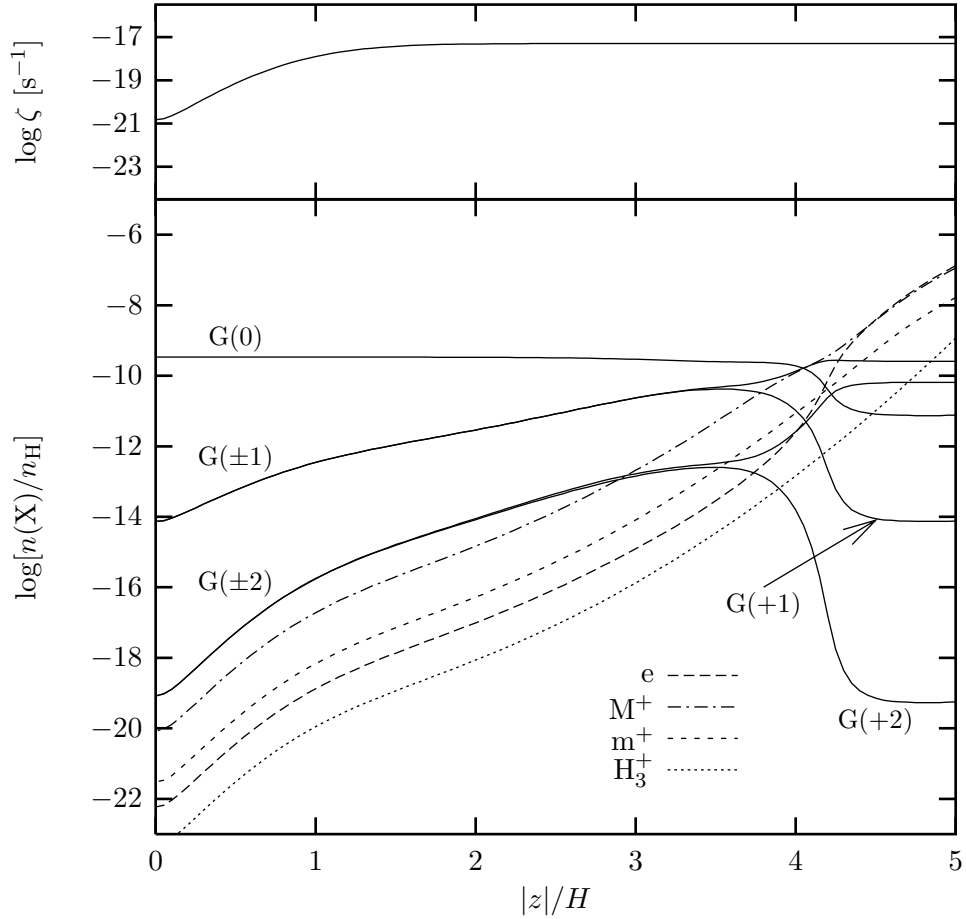


Fig. 13.— Relative abundances  $n(X)/n_H$  of some representative particles as functions of the height  $|z|$  from the midplane at  $r = 1$  AU for the MRN size distribution of grains. The other parameters are the same as those of the fiducial model. The upper panel shows the ionization rate  $\zeta$ .

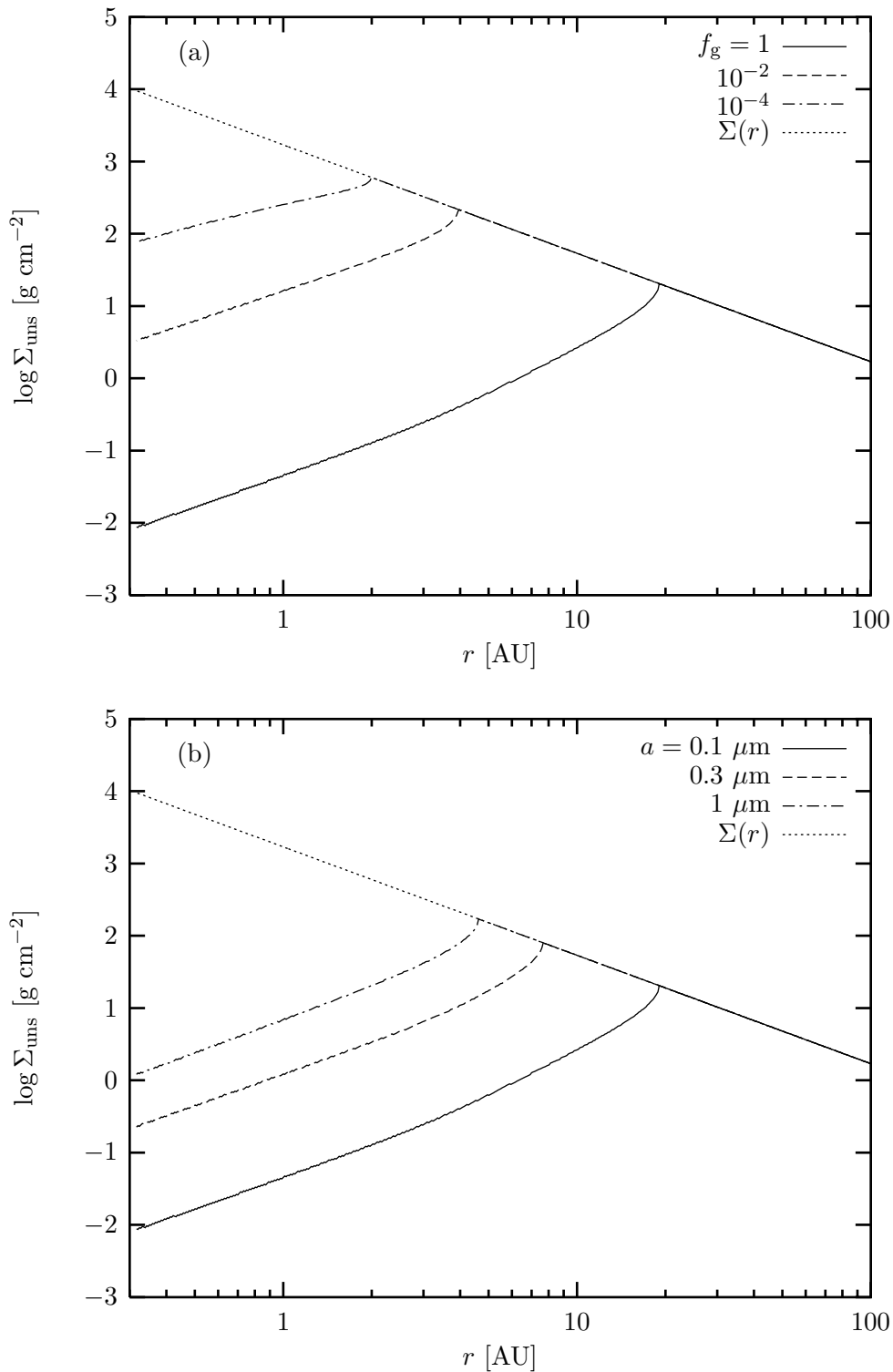


Fig. 14.— The column density of the unstable layer,  $\Sigma_{\text{uns}}$ , (a) for the models of grain depletion  $f_g = 1$ ,  $10^{-2}$ , and  $10^{-4}$ , and (b) for the models of grain radius  $a = 0.1$ ,  $0.3$ , and  $1 \mu\text{m}$ . The other parameters are the same as those of the fiducial model.

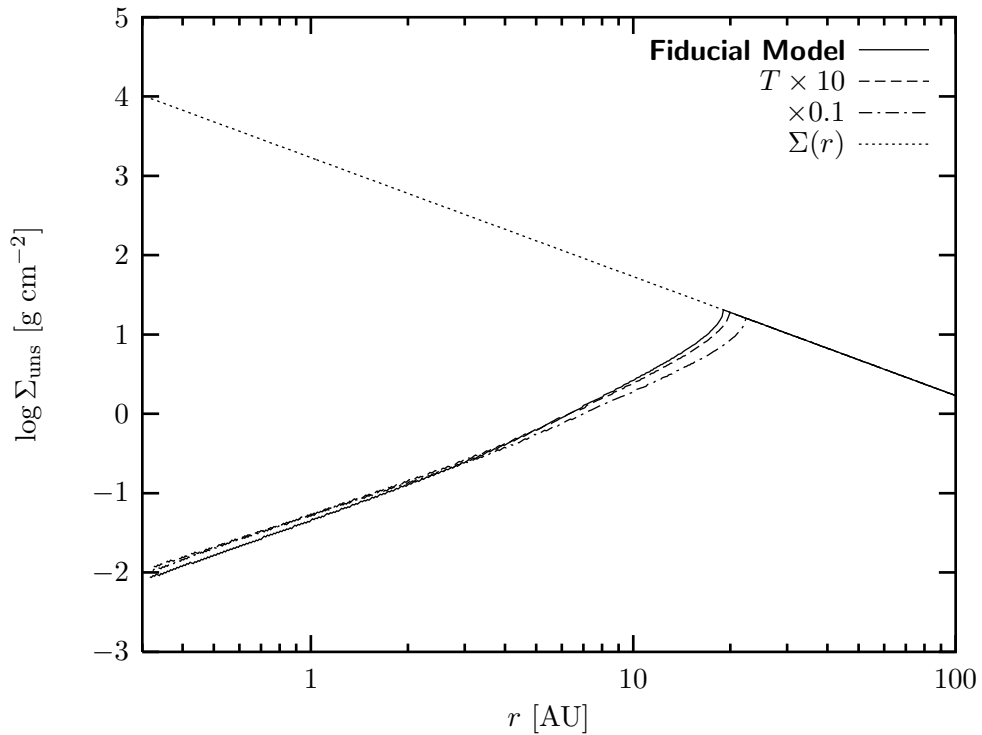


Fig. 15.— The column density of the unstable layer,  $\Sigma_{\text{uns}}$ , for the models with temperature 10 times higher (*dashed curve*) and 10 times lower (*dot-dashed curve*) than the fiducial model (*solid curve*). The other parameters are the same as those of the fiducial model.

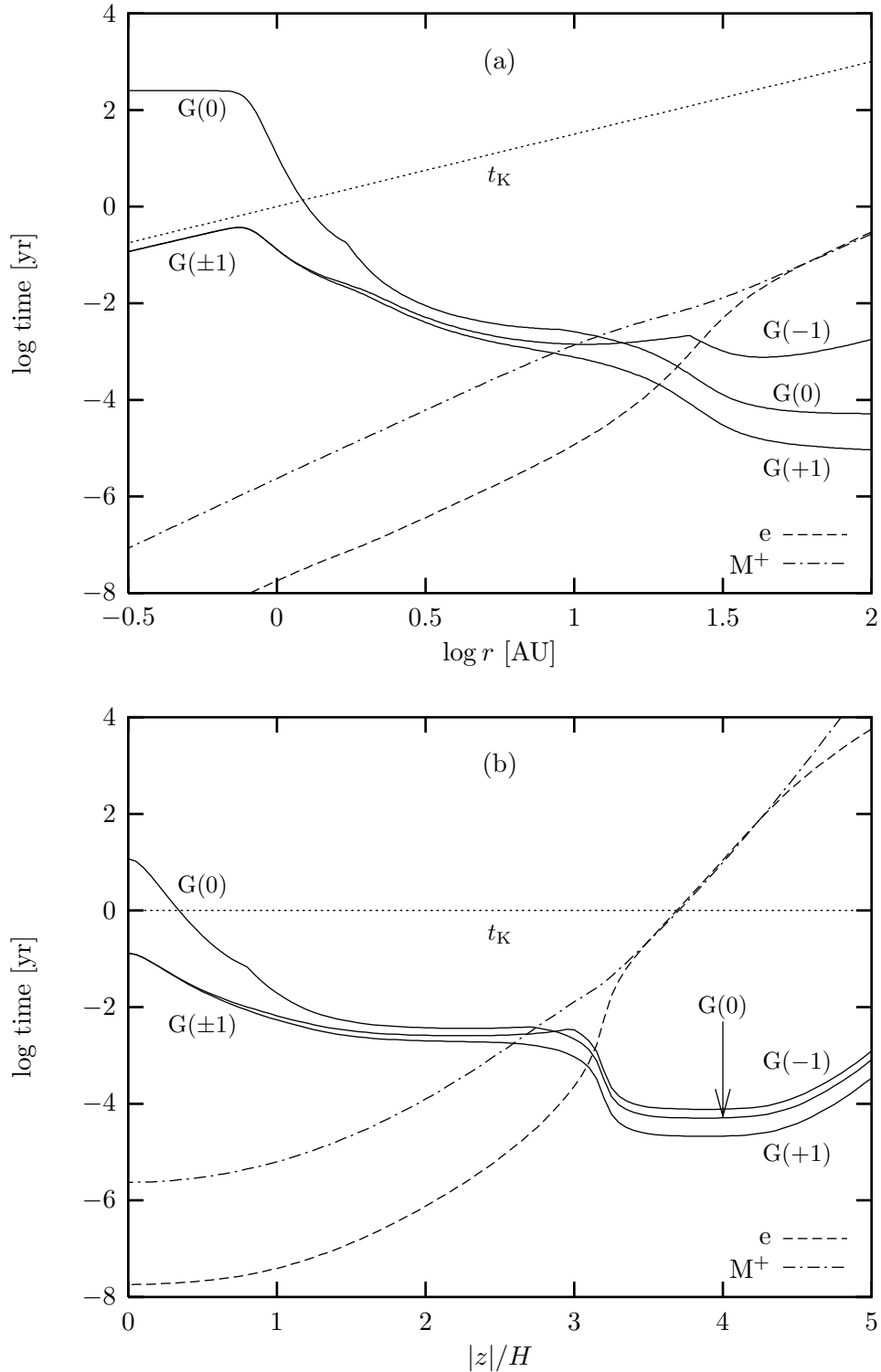


Fig. 16.— The relaxation time  $t_r$  to the ionization-recombination equilibrium for some representative particles (a) on the midplane as functions of  $r$ , and (b) at  $r = 1$  AU as functions of  $|z|$ , for the fiducial model. The Keplerian orbital period  $t_K$  is also shown by the dotted line.

Table 1. Abundance of Elements and their Fraction in the Gas Phase

Element	Abundance	Chemical Species	Fraction in Gas Phase
H	1	H <sub>2</sub>	1
He	$9.75 \times 10^{-2}$	He	1
C	$3.62 \times 10^{-4}$	CO	$\delta_1$
O	$8.53 \times 10^{-4}$	O <sub>2</sub> ,O	$\delta_1$
Metal Total	$7.97 \times 10^{-5}$	M	$\delta_2$

Table 2. Two-Body Reactions and their Rate Coefficients

Reaction					Rate coefficient (cm <sup>3</sup> s <sup>-1</sup> )
H <sup>+</sup>	+	Mg	→	Mg <sup>+</sup> + H	$1.10 \times 10^{-9}$
H <sup>+</sup>	+	O	→	O <sup>+</sup> + H	$7.00 \times 10^{-10} \exp(-232.0/T)$
H <sup>+</sup>	+	O <sub>2</sub>	→	O <sub>2</sub> <sup>+</sup> + H	$2.00 \times 10^{-9}$
H <sub>2</sub> <sup>+</sup>	+	H <sub>2</sub>	→	H <sub>3</sub> <sup>+</sup> + H	$2.08 \times 10^{-9}$
H <sub>3</sub> <sup>+</sup>	+	O	→	OH <sup>+</sup> + H <sub>2</sub>	$8.00 \times 10^{-10}$
H <sub>3</sub> <sup>+</sup>	+	Mg	→	Mg <sup>+</sup> + H + H <sub>2</sub>	$1.00 \times 10^{-9}$
H <sub>3</sub> <sup>+</sup>	+	CO	→	HCO <sup>+</sup> + H <sub>2</sub>	$1.70 \times 10^{-9}$
H <sub>3</sub> <sup>+</sup>	+	O <sub>2</sub>	→	O <sub>2</sub> H <sup>+</sup> + H <sub>2</sub>	$5.00 \times 10^{-9} \exp(-150.0/T)$
He <sup>+</sup>	+	H <sub>2</sub>	→	H <sup>+</sup> + H + He	$3.70 \times 10^{-14} \exp(-35.0/T)$
He <sup>+</sup>	+	CO	→	C <sup>+</sup> + O + He	$1.60 \times 10^{-9}$
He <sup>+</sup>	+	O <sub>2</sub>	→	O <sup>+</sup> + O + He	$1.00 \times 10^{-9}$
C <sup>+</sup>	+	Mg	→	Mg <sup>+</sup> + C	$1.10 \times 10^{-9}$
C <sup>+</sup>	+	H <sub>2</sub>	→	CH <sub>2</sub> <sup>+</sup> + hν	$4.00 \times 10^{-16} (T/300)^{-0.20}$
C <sup>+</sup>	+	O <sub>2</sub>	→	CO <sup>+</sup> + O	$3.80 \times 10^{-10}$
C <sup>+</sup>	+	O <sub>2</sub>	→	O <sup>+</sup> + CO	$6.20 \times 10^{-10}$
HCO <sup>+</sup>	+	Mg	→	Mg <sup>+</sup> + HCO	$2.90 \times 10^{-9}$
H <sup>+</sup>	+	e	→	H + hν	$3.50 \times 10^{-12} (T/300)^{-0.75}$
H <sub>3</sub> <sup>+</sup>	+	e	→	H <sub>2</sub> + H	$1.50 \times 10^{-8} (T/300)^{-0.50}$
H <sub>3</sub> <sup>+</sup>	+	e	→	H + H + H	$1.50 \times 10^{-8} (T/300)^{-0.50}$
He <sup>+</sup>	+	e	→	He + hν	$2.36 \times 10^{-12} (T/300)^{-0.64}$
C <sup>+</sup>	+	e	→	C + hν	$4.40 \times 10^{-12} (T/300)^{-0.61}$
Mg <sup>+</sup>	+	e	→	Mg + hν	$2.80 \times 10^{-12} (T/300)^{-0.86}$
HCO <sup>+</sup>	+	e	→	CO + H	$1.10 \times 10^{-7} (T/300)^{-1.00}$



Table 3. Ionization Rates

Reaction	Rate
$\text{H}_2 \rightarrow \text{H}_2^+ + \text{e}$	$0.97\zeta^{\text{a}}$
$\text{H}_2 \rightarrow \text{H}^+ + \text{H} + \text{e}$	$0.03\zeta$
$\text{He} \rightarrow \text{He}^+ + \text{e}$	$0.84\zeta$

<sup>a</sup> $\zeta$  is the total ionization rate for a hydrogen molecule.